

This is the peer reviewed version of the following article:

Tribology of HVOF- and HVOF-sprayed WC-10Co4Cr hardmetal coatings: A comparative assessment / Bolelli, Giovanni; Berger, L. M.; Börner, T.; Koivuluoto, H.; Lusvarghi, Luca; Lyphout, C.; Markocsan, N.; Matikainen, V.; Nylén, P.; Sassatelli, Paolo; Trache, R.; Vuoristo, P.. - In: SURFACE & COATINGS TECHNOLOGY. - ISSN 0257-8972. - ELETTRONICO. - 265:(2015), pp. 125-144. [10.1016/j.surfcoat.2015.01.048]

*Terms of use:*

The terms and conditions for the reuse of this version of the manuscript are specified in the publishing policy. For all terms of use and more information see the publisher's website.

05/01/2026 18:58

## Accepted Manuscript

Tribology of HVOF- and HVOF-sprayed WC-10Co4Cr hardmetal coatings: a comparative assessment

G. Bolelli, L.-M. Berger, T. Börner, H. Koivuluoto, L. Lusvarghi, C. Lyphout, N. Markocsan, V. Matikainen, P. Nylén, P. Sassatelli, R. Trache, P. Vuoristo

PII: S0257-8972(15)00082-1  
DOI: doi: [10.1016/j.surfcoat.2015.01.048](https://doi.org/10.1016/j.surfcoat.2015.01.048)  
Reference: SCT 20063

To appear in: *Surface & Coatings Technology*

Received date: 10 September 2014  
Accepted date: 20 January 2015



Please cite this article as: G. Bolelli, L.-M. Berger, T. Börner, H. Koivuluoto, L. Lusvarghi, C. Lyphout, N. Markocsan, V. Matikainen, P. Nylén, P. Sassatelli, R. Trache, P. Vuoristo, Tribology of HVOF- and HVOF-sprayed WC-10Co4Cr hardmetal coatings: a comparative assessment, *Surface & Coatings Technology* (2015), doi: [10.1016/j.surfcoat.2015.01.048](https://doi.org/10.1016/j.surfcoat.2015.01.048)

This is a PDF file of an unedited manuscript that has been accepted for publication. As a service to our customers we are providing this early version of the manuscript. The manuscript will undergo copyediting, typesetting, and review of the resulting proof before it is published in its final form. Please note that during the production process errors may be discovered which could affect the content, and all legal disclaimers that apply to the journal pertain.

**Tribology of HVOF- and HVOF-sprayed WC-10Co4Cr hardmetal coatings: a comparative assessment**

G. Bolelli<sup>1),\*</sup>, L.-M. Berger<sup>2) a)</sup>, T. Börner<sup>1,2) b)</sup>, H. Koivuluoto<sup>3)</sup>, L. Lusvarghi<sup>1)</sup>, C. Lyphout<sup>4)</sup>,  
N. Markocsan<sup>4)</sup>, V. Matikainen<sup>3)</sup>, P. Nylén<sup>4)</sup>, P. Sassatelli<sup>1)</sup>, R. Trache<sup>2)</sup>, P. Vuoristo<sup>3)</sup>

<sup>1)</sup> Dipartimento di Ingegneria “Enzo Ferrari”, University of Modena and Reggio Emilia, Via Vignolese 905, I-41125 Modena (MO), Italy

<sup>2)</sup> Fraunhofer-Institut für Werkstoff- und Strahltechnik (IWS), Winterbergstr. 28, D-01277 Dresden, Germany

<sup>3)</sup> Department of Materials Science, Tampere University of Technology, Korkeakoulunkatu 6, FI-33720 Tampere, Finland

<sup>4)</sup> Department of Engineering Science, University West, Gustava Melins gata 2, SE-461 86 Trollhättan, Sweden

<sup>a)</sup> Present address: Fraunhofer-Institut für Keramische Technologien und Systeme (IKTS)

<sup>b)</sup> Present address: Institut für Korrosionsschutz Dresden GmbH

\* Corresponding author: tel.: +39 059 2056233; fax: +39 059 2056243;

e-mail: giovanni.bolelli@unimore.it

**Abstract**

This paper provides a comprehensive assessment of the sliding and abrasive wear behaviour of WC-10Co4Cr hardmetal coatings, representative of the existing state-of-the-art. A commercial feedstock powder with two different particle size distributions was sprayed onto carbon steel substrates using two HVOF and two HVOF spray processes.

Mild wear rates of  $<10^{-7} \text{ mm}^3/(\text{Nm})$  and friction coefficients of  $\approx 0.5$  were obtained for all samples in ball-on-disk sliding wear tests at room temperature against  $\text{Al}_2\text{O}_3$  counterparts. WC-10Co4Cr coatings definitely outperform a reference electrolytic hard chromium coating under these test conditions. Their wear mechanisms include extrusion and removal of the binder matrix, with the formation of a wavy surface morphology, and brittle cracking. The balance of such phenomena is closely related to intra-lamellar features, and rather independent of those properties (e.g. indentation fracture toughness, elastic modulus) which mainly reflect large-scale inter-lamellar cohesion, as quantitatively confirmed by a principal component analysis. Intra-lamellar dissolution of WC into the matrix indeed increases the incidence of brittle cracking, resulting in slightly higher wear rates. At  $400^\circ\text{C}$ , some of the hardmetal coatings fail because of the superposition between tensile residual stresses and thermal expansion mismatch stresses (due to the difference between the thermal expansion coefficients of the steel substrate and of the hardmetal coating). Those which do not fail, on account of lower residual stresses, exhibit higher wear rates than at room temperature, due to oxidation of the WC grains.

The resistance of the coatings against abrasive wear, assessed by dry sand-rubber wheel testing, is related to inter-lamellar cohesion, as proven by a principal component analysis of the collected dataset. Therefore, coatings deposited from coarse feedstock powders suffer higher wear loss than those obtained from fine powders, as brittle inter-lamellar detachment is caused by their weaker interparticle cohesion, witnessed by their systematically lower fracture toughness as well.

*Key-words: Hardmetal; WC-10Co4Cr; High Velocity Oxy-Fuel (HVOF); High Velocity Air-Fuel (HVOF); sliding wear; abrasive wear*

## 1. Introduction

Hardmetal coatings deposited by the high velocity oxy-fuel (HVOF) spray process exhibit high density and mechanical strength. This results from the high momentum of the feedstock powder particles at the moment of impact on the substrate [1] and from their significantly lower temperature, much more suitable to hardmetal compositions than that attained e.g. in atmospheric plasma spraying (APS) processes. These coatings accordingly find a large variety of industrial applications for the protection of mechanical components against sliding and abrasive wear at various temperatures [2] and in different environments. They are also listed among the most promising alternatives to hard chromium electroplating [3], due to their technical advantages [3,4] coupled to the lower environmental and lifecycle impact of the deposition process [5]. This is of particular interest as the chromium electroplating technique is facing regulatory restrictions due to its environmental and health hazardousness [6,7].

The properties of thermal spray hardmetal coatings, including their wear resistance in different tribological conditions, may however vary as a function of the feedstock powder properties, the spray process, and the deposition parameters, as shown e.g. by a number of studies on WC-based materials [8-12]. From these studies, it is inferred that some of the most influential factors include the selection of the HVOF spray process (among the many commercially available ones) [1,8-11], the process parameters [10,13], the properties of the carbide (WC- or  $\text{Cr}_3\text{C}_2$ -based) and the binder phase, as well as the composition and the properties of the feedstock powder (size of particles [13-15] and of carbide grains [16-18]). Specifically, the need to heat powder particles enough to achieve plastic deformation of the feedstock powder particles at the moment of impact, and, consequently, good inter-lamellar bonding must be balanced with the contrasting need to prevent changes of the chemical and phase composition [19]. This means a certain degree of decarburisation is unavoidable when using the HVOF process.

In addition to the HVOF processes, the high velocity air-fuel (HVOF) process was developed nearly in the same period of time [20]. Due to low deposition efficiencies of the first generations of spray guns, this process did not find wide distribution in the industry.

Significant constructive enhancements about 15 years ago increased the economic effectiveness. Together with lower thermal load and the higher velocities of the feedstock powder particles, this spray process represents an alternative to the HVOF spray processes. This broadens the range of available choices by offering the possibility to deposit dense coatings with excellent mechanical properties and high wear resistance [19].

Nowadays, the composition WC – 10 wt.% Co – 4 wt.% Cr (designated as WC-10Co4Cr in the following) is one of the most important commercially available ones and widely used for the preparation of coatings having simultaneously high wear and corrosion resistance [12].

Intensive studies on this composition have started end of 1990-ies only [21] and were closely connected with the increasing use of HVOF sprayed coatings [12]. The ratio of cobalt to chromium in this composition is 2:1 by volume and the nominal content of carbon is 5.27% [22]. WC, the  $\eta$ -phase  $(\text{Co,Cr})_3\text{W}_3\text{C}$ , and a  $(\text{Co,Cr,W})$  alloy binder are expected to be in thermodynamic equilibrium. However, in the case of higher carbon content, in equilibrium conditions a  $(\text{Co,Cr,W})_7\text{C}_3$  phase will appear instead of the  $\eta$ -phase [22,23]. In all cases, chromium is contained both in the metallic binder and the hard phase [22-24]. Another important feature of chromium addition is a significant melting point reduction compared to plain WC-Co [23]. In general, it seems that WC-10Co4Cr is a good empirically derived and balanced formulation for the preparation of simultaneous wear and corrosion resistant coatings [22].

Under sliding and abrasive wear conditions, properly manufactured WC-based hardmetal coatings exhibit matrix abrasion, until unsupported WC grains are fractured and/or pulled out of the surface [25,26]. Microscale plastic deformation of the top surface has also been noted after sliding wear testing in some studies [27-29]. In case of excessive changes of phase

composition, the coatings reportedly become very brittle, with surface and sub-surface crack propagation dominating their tribological behaviour in sliding and abrasive conditions [11,16-18,30,31]. When particles are scarcely heated during spraying, by contrast, inter-lamellar detachment is likely to occur [31].

Many of the cited papers, however, consider a limited set of coatings, which do not allow a comprehensive assessment of different technologies and different feedstock powders. Even those which report about systematic studies, such as the literature on the comparison between HVOF- and HVAF-sprayed WC-based hardmetal coatings [11,32-34], have limitations, such as the description of samples not belonging to the state-of-the-art due to the use of older deposition technologies and/or of non-optimal parameters, or the lack of a detailed investigation of wear mechanisms. Little information is also available on the high temperature wear behaviour of WC-based hardmetal coatings (few examples are given in [28,29,35,36]). The present research therefore aims to provide a comprehensive assessment of the tribological properties of HVOF- and HVAF-sprayed WC-10Co4Cr hardmetal coatings obtained by the use of feedstock powders with different particle size distributions. These coatings provide a representative picture of the state-of-the-art. Focus is made on the characterisation of the wear behaviour under dry sliding wear (at room temperature and at 400 °C) and abrasive wear conditions.

## **2. Experimental**

### *2.1 Sample manufacturing*

One commercial powder composition (WC-10Co4Cr), with two different particle size distributions suitable for the HVOF and HVAF spray processes, was provided by one manufacturer and sprayed using four different thermal spray techniques: a liquid-fuelled (paraffine) JP-5000 HVOF spray process (Praxair-TAFA, Concord, NH, USA), a gas-fuelled (propane) Diamond Jet 2700 HVOF spray process (Sulzer-Metco, Wohlen, Switzerland), and

the M2 and M3 HVAF spray processes (Uniquecoat Technologies llc., Oilville VA, USA). The latter differ both in torch construction and in the employed fuels, respectively methane and propane. A summary of all powders, processes and coatings employed in this study, together with their conventional designations used hereafter, is provided in Table I.

All coatings were sprayed onto 100 x 50 x 8 mm plates of low-carbon Domex 355 steel (chemical composition, in weight %: C < 0.10, Mn = 1.50, P < 0.025, S < 0.010, Fe = balance), which were grit-blasted before deposition. The samples were mounted on a rotating sample holder; the resulting coatings had a thickness of  $\approx 250 - 300 \mu\text{m}$ . Process parameters for all deposition techniques had previously been optimised in order to obtain dense coatings with high deposition efficiency.

As a term of comparison, two electroplated hard chromium layers (both  $\approx 300 \mu\text{m}$  thick) were deposited at an industrial facility onto the same plates (subjected to a preliminary grinding process according to the manufacturer's standard procedures), using a conventional  $\text{CrO}_3 + \text{H}_2\text{SO}_4$  Fink's electroplating bath with proprietary additives.

## 2.2 Microstructural characterisation

The cross-sectional microstructure of the coatings and of the feedstock powders was characterised by scanning electron microscopy (SEM: Philips XL30 and Quanta-200, FEI, Eindhoven, NL) equipped with energy-dispersive X-ray (EDX) microanalysis (DX-4 EDAX, USA and Inca, Oxford Instruments Analytical, Abingdon, UK). Both the powders and the coated samples were cold-mounted in epoxy resin, ground with diamond papers (up to 1200 mesh) and polished with diamond slurries ( $6 \mu\text{m}$  and  $3 \mu\text{m}$ ) and colloidal silica suspension.

Image analysis was performed on SEM micrographs of the coatings cross sections, obtained using a TM3000-Tabletop Microscope (HITACHI), in order to determine the volume fraction



of pores and of carbide grains and the size of the latter in each sample. A specially developed image thresholding algorithm utilizing the Aphelion® image analysis software was applied on 20 SEM pictures (7000x magnification) per sample.

The phase composition of the feedstock powders and of all coatings was assessed by X-ray diffraction (XRD: Empyrean, PANALYTICAL, Almelo, NL), performed with Cu-K $\alpha$  radiation in the  $20^\circ \leq 2\theta \leq 120^\circ$  range. The integral intensities of the (100) peak of WC ( $I_{WC}$ ) and of the (101) peak of W<sub>2</sub>C ( $I_{W_2C}$ ) were assessed by pattern fitting using pseudo-Voigt functions and the index of carbide retention ( $I$ ), quantifying the retention of the WC phase against the formation of W<sub>2</sub>C, was computed as  $I = I_{WC} / (I_{WC} + I_{W_2C})$ , according to the definition in [10].

In addition, both fractions of the feedstock powder were analysed for their total carbon content by the combustion method (WC 600, LECO Corporation, St. Joseph, MI, USA) and for their magnetic saturation (Sigmameter, Setaram, Saint-Cloud, France). The latter method allows to obtain fast additional information about the state of cobalt in the hardmetal composition, in combination with XRD results, and it is described in more detail elsewhere [22].

The microhardness of the coatings was measured on polished cross-sections by Vickers indentation according to the standard ASTM E-384-10. Measurements were carried out using a Vickers indenter (Shimadzu Microhardness Tester) at three different loads of 100 gf ( $\approx 1$  N), 300 gf ( $\approx 3$  N) and 500 gf ( $\approx 5$  N), with a dwell time of 15 s. For each load, 20 impressions, evenly distributed in a half circle through the entire test panel, were made on each coating cross section.

Indentation fracture toughness (IFT) was also assessed by performing indentations into the polished cross-sections of the coatings using a Vickers-shaped indenter (12 indents, Mitutoyo AVK C1). A high peak load of 5 kgf ( $\approx 49$  N, load period 10 s) was employed in order to induce crack propagation from the indent corners. Fracture toughness was determined by

measuring crack lengths on optical micrographs (200x magnification, 2560 x 1920 pixel resolution) using ImageJ [37]. Only cracks parallel to the substrate starting at the left and right tip of indents, respectively, were considered (Figure 1), according to the method described in [38]. The critical stress intensity ( $K_{IC}$ ) was calculated according to Niihara et al. [39] based on the Palmqvist crack model.

The Young's modulus has been measured with the surface acoustic wave method (LAwave®), the details of sample preparation and measurement technique are given elsewhere [40,41].

In order to determine the thermal expansion coefficient of the WC-10Co4Cr coating and of the steel substrate, optical dilatometer measurements (Horizontal Optical Dilatometer Misura® ODLT, Expert System Solutions, Modena, Italy) were performed on 50 x 5 x 0.3 mm specimens obtained from sample P2W1 by metallographic cutting and grinding with SiC papers. Measurements were carried out in air at a heating rate of 5 °C/min up to 400 °C. Two heating cycles were performed and the thermal expansion coefficient values were obtained from the second cycle, in order to avoid artefacts due e.g. to the release of residual stresses, in accordance with the procedure described in [42].

### 2.3 Wear testing

Rotating ball-on-disk tests (High Temperature Tribometer, CSM Instruments, Peseux, Switzerland) were performed according to the ASTM G99 standard on ground and polished coating surfaces ( $R_a \approx 0.02 \mu\text{m}$ ). The stationary counterparts were sintered  $\text{Al}_2\text{O}_3$  spheres (nominal hardness  $\text{HV} \approx 1900$ ) of 6 mm diameter. Test conditions include normal load of 10 N, relative sliding speed of 0.10 m/s, wear track radius of 7 mm and an overall sliding distance of 5000 m. Tests were performed both at room temperature (temperature  $\approx 25 \text{ }^\circ\text{C}$ , relative humidity  $\approx 60\%$ ) and at 400 °C. In the latter case, the samples were induction heated

from the base plate of the tribometer and their temperature was monitored by a thermocouple in contact with their rear surface. The samples were heated for 1 h up to 400 °C and they were allowed for additional 30 min to stabilize in isothermal conditions. At least two tests were performed for each coating.

The friction coefficient was monitored during the test using a load cell attached to the ball holding arm. The volume losses of samples and counterparts were assessed by optical confocal profilometry (Conscan profilometer, CSM Instruments) of wear tracks and by optical microscopy measurement of worn cap diameters, respectively. Data were normalised over sliding distance and normal load in order to obtain the wear rates.

Moreover, the morphology of the wear scars on the samples was studied by SEM. The phase composition of the debris clusters attached to the wear scar and of the loose debris particles laying outside the wear scar was assessed by micro-Raman spectroscopy (LabRam, Horiba Jobin-Yvon, Villeneuve d'Ascq, France) using a 632.81 nm-wavelength He:Ne laser radiation focused through 50x and 100x objectives. Some representative samples of loose debris particles were also collected on a Cu grid for observation by transmission electron microscope (TEM: JEM 2010, Jeol, Tokio, Japan), equipped with EDX microanalysis detector (INCA).

Abrasion wear behaviour of the coatings was evaluated using a modified version of the ASTM G65 dry sand-rubber-wheel (DSRW) abrasion wear test, where five samples were tested simultaneously. Blocky-shaped dry quartz sand ( $\text{SiO}_2$ ) with a grain size ranging from 0.1 to 0.6 mm was used as the abrasive. The flow rate of the abrasive was 25 g/min. Sample surfaces were ground using 1200 grit SiC paper ( $R_a \approx 8\mu\text{m}$ ) before testing. During the test, the samples were pressed with a normal load of 23 N against a rotating rubber wheel with a surface speed of 1.64 m/s. The test lasted for 60 min for an overall wear distance of 5904 m. The samples were weighed every 12 min using an analytical scale with 0.001g accuracy, in order to determine their mass loss, which was converted to volume loss using density values.

Specifically, the density of each hardmetal coating was computed based on its volume fraction of pores and carbide grains determined by image analysis (Section 2.2), using  $\rho_{WC} = 15.7 \text{ g/cm}^3$  as the density of WC and  $\rho_{binder} = 8.6 \text{ g/cm}^3$  [43] as the density of the binder matrix (in the absence of precise data, the latter value was assumed to be approximately equal to that of a Stellite® alloy). Some of the coatings contained significant amounts of  $W_2C$ , which has a higher density ( $17.2 \text{ g/cm}^3$ ) than WC. However, the error for the conversion into volume loss made by neglecting these amounts of  $W_2C$  has been estimated to be smaller than the error of the measurement. The density of electrolytic hard chromium was assumed to be  $\rho_{EHC} = 7.2 \text{ g/cm}^3$  [44].

Worn surfaces were also observed by SEM (XL40, FEI).

#### 2.4 Residual stress measurements

Residual stresses were measured by X-ray diffraction (X'Pert PRO diffractometer, PANALytical, Almelo, NL; Cu-K $\alpha$  radiation) on as-deposited samples P1W1, P2W1, P3W1 and P4W1 (Table I).

Measurements were performed according to the  $\sin^2\psi$  method in  $\omega$ -tilt configuration. A line focus source with parallel beam set-up, comprising an X-ray mirror on the incident beam path and a gas-proportional detector with parallel plate collimator on the diffracted beam path, was employed in order to minimise errors due to sample positioning in the vertical direction [45,46].

The (211) peak of WC, located at  $2\theta \approx 117.3^\circ$ , was acquired with a  $2\theta$  scan range of  $4^\circ$ . Measurements were performed at symmetric positive as well as pseudo-negative  $\psi$  angles corresponding to  $\sin^2\psi$  values of 0, 0.1, ..., 0.4, and they were repeated at three different sample orientation angles ( $\phi$ ) of  $0^\circ$ ,  $45^\circ$  and  $90^\circ$ , where  $\phi = 0^\circ$  and  $\phi = 90^\circ$  correspond to the

directions parallel to the major and minor side of the rectangular samples, respectively. The interplanar spacing  $d_{\varphi,\psi}^{(211)}$  was therefore obtained at each  $\psi, \varphi$  position and the corresponding lattice strain was computed as  $\varepsilon_{\varphi,\psi}^{(211)} = (d_{\varphi,\psi}^{(211)} - d_0^{(211)})/d_0^{(211)}$ , where  $d_0^{(211)}$  is the unstressed interplanar spacing. According to [47], assuming a plane stress condition, the  $\sin^2\psi$  equation can be written for the three  $\varphi$  orientations to yield the following relations (1):

$$\varepsilon_{0^\circ,\psi}^{(211)} = \frac{1}{2}S_2^{(211)}\sigma_{11}\sin^2\psi + S_1^{(211)}(\sigma_{11} + \sigma_{22}) \quad (1.1)$$

$$\varepsilon_{90^\circ,\psi}^{(211)} = \frac{1}{2}S_2^{(211)}\sigma_{22}\sin^2\psi + S_1^{(211)}(\sigma_{11} + \sigma_{22}) \quad (1.2)$$

$$\varepsilon_{45^\circ,\psi}^{(211)} = \frac{1}{2}S_2^{(211)}\left(\frac{\sigma_{11}+\sigma_{22}}{2} + \tau_{12}\right)\sin^2\psi + S_1^{(211)}(\sigma_{11} + \sigma_{22}) \quad (1.3)$$

The normal stress components  $\sigma_{11}$  and  $\sigma_{22}$  are therefore obtained from the slopes of the linear plots of  $\varepsilon_{\varphi,\psi}^{(211)}$  vs.  $\sin^2\psi$  for  $\varphi = 0^\circ$  and  $\varphi = 90^\circ$ , respectively (1.1 and 1.2). Using these values together with the slope of the plot for  $\varphi = 45^\circ$ , the in-plane shear stress component  $\tau_{12}$  is then obtained according to (1.3).

The elastic constants of WC along the (211) direction are  $\frac{1}{2}S_2^{(211)} = 2.44 \cdot 10^{-6} \text{ MPa}^{-1}$  and  $S_1^{(211)} = -4.10 \cdot 10^{-7} \text{ MPa}^{-1}$ , respectively [48].

The unstressed lattice spacing  $d_0^{(211)}$  is not known *a priori*: it is possible to replace its value by the interplanar spacing measured at  $\psi = 0^\circ$ , i.e. assuming  $d_0^{(211)} \approx d_{\varphi,\psi=0^\circ}^{(211)}$ , with a limited error (not greater than 1% [49]). The result, however, is further refined by an iterative procedure. By setting  $\psi = 0^\circ$  in equation (1), it follows:

$$\frac{d_{\varphi,\psi=0^\circ}^{(211)} - d_0^{(211)}}{d_0^{(211)}} = \varepsilon_{\varphi,\psi=0^\circ}^{(211)} = S_1^{(211)}(\sigma_{11} + \sigma_{22}) \rightarrow d_0^{(211)} = \frac{d_{\varphi,\psi=0^\circ}^{(211)}}{1 + S_1^{(211)}(\sigma_{11} + \sigma_{22})} \quad (2)$$

The values of  $\sigma_{11}$ ,  $\sigma_{22}$  and  $\tau_{12}$  first obtained in the hypothesis that  $d_0^{(211)} \approx d_{\varphi, \psi=0^\circ}^{(211)}$  are therefore adjusted by re-calculating  $d_0^{(211)}$  with equation (2) until convergence is reached.

### 3. Results and discussion

#### 3.1 Feedstock powder characterisation

The feedstock powders W1 and W2 appear very dense (Figure 2A-D), with small WC grains, producing a bright contrast in these SEM micrographs, and some large dark grey areas. The diffraction peaks in XRD pattern of the feedstock powders, presented together with those of the coatings in Figure 3, indicate the presence of at least one more phase, apart from WC and metallic f.c.c.-Co. In order to determine the composition of the dark grey areas which are probably associated with this phase, the result of the EDX microanalysis are displayed in Figure 2E for the area marked in Figure 2C. These dark areas, containing cobalt and chromium as main components together with very few tungsten, most probably correspond to a  $(\text{Co,Cr,W})_7\text{C}_3$  carbide. According to a short summary of phase formation for the WC-10Co4Cr composition [22], above the solubility limit of chromium in the binder at high carbon content  $(\text{Co,Cr,W})_7\text{C}_3$  carbides can be formed. The results of the experimental study of Zackrisson et al. [50] and a study on the effect of chromium on phase equilibria in WC-Co hardmetals by Frisk and Markström [23] have shown similar results. It should be mentioned that the  $(\text{Co,Cr,W})_7\text{C}_3$  phase is difficult to distinguish from the f.c.c.-Co and from the  $\eta$ -phase ( $\text{M}_6\text{C}$ ) in the X-ray diffraction pattern. The position of the two main diffraction peaks of  $\text{Cr}_7\text{C}_3$  (respectively located at  $2\theta = 44.2^\circ$  and  $2\theta = 42.5^\circ$  according to the JCPDF 36-1482 file) are very close to those of f.c.c.-Co ( $2\theta = 44.2^\circ$ , JCPDF 15-806) and of the  $\eta$ -phase ( $2\theta = 42.4^\circ$ , JCPDF 27-1125), and some peak shift due to Co and W substituting for Cr in the  $\text{M}_7\text{C}_3$  lattice may further enhance the overlapping. Such dark areas were found also in the cross sections of other commercial agglomerated and sintered WC-10Co4Cr feedstock powders, published elsewhere [51-53].

The total carbon content was 5.45 wt.% and 5.44 wt.% for the W1 and W2 powders, respectively. Both values are significantly higher than the nominal content of 5.27 wt.% in the composition WC-10Co4Cr. This is an additional indication of the existence of  $(\text{Co,Cr,W})_7\text{C}_3$  in the feedstock powder. All feedstock powders produced by sintering and crushing, studied earlier [22], had a total carbon content below the nominal carbon content, and thus contained the  $\eta$ -phase instead.

The magnetic saturation was  $7.5 \mu\text{Tm}^3/\text{kg}$  and  $8.1 \mu\text{Tm}^3/\text{kg}$  for the W1 and W2 powders, respectively. These values are of the same order of magnitude as those measured on sintered and crushed feedstock powders with a carbon content below the nominal one [22]. When the carbon content is above the nominal value, cobalt is largely contained in the  $(\text{Co,Cr,W})_7\text{C}_3$  phase as discussed previously, whereas it enters the  $\eta$ -phase when the carbon content is below the nominal value: in both cases, therefore, only a limited amount of metallic cobalt is left in the matrix. In addition, the magnetic saturation of this metallic cobalt might be decreased by some dissolved chromium.

### 3.2 Coating microstructures

All coatings have thicknesses of 250 – 300  $\mu\text{m}$ , as expected (Section 2.1). They exhibit macroscopically dense microstructures (Figure 4A,C,E,G) with low porosity detectable at these magnifications. At greater magnifications, some pores (producing black contrast in backscattered electron imaging mode) become visible (Figure 4B,D,F,H). Specifically, image analysis showed (Table II) that the fine feedstock powder results in less porous coatings (W1-series) than the coarse one (W2-series), although the scatter of the experimental data is quite large.

In greater detail, the coatings deposited by the HVOF processes (P2- and P3-series: Figure 4D,F) differ from those deposited by HVAF processes (P1- and P4-series: Figure 4B,H). In

the latter, due to the low HVOF process temperatures, the changes to the chemical and phase compositions were minimal or absent, also all of the WC grains contained in the feedstock powders (Figure 2A-D), including the finest (sub-micrometric) ones, are found in the coating (Figure 4B,H) and they exhibit the same, angular morphology. In the HVOF-sprayed coatings, due to the higher process temperature a higher degree of melting and more intensive metallurgical reactions occur, accompanied with a more intense carbon loss. This leads to the disappearance of the dark grey  $(\text{Co,Cr,W})_7\text{C}_3$  grains (Figure 4D,F). Moreover, qualitative inspection of the SEM micrographs indicates that some of the finest carbide grains were partly lost and the remaining ones exhibit more rounded edges, as a consequence of decarburisation and/or of dissolution in the molten matrix (Figure 4D,F). Accordingly, the matrix phase acquires a brighter backscattered electrons contrast level in splats where WC dissolution was more pronounced. The alteration of WC grains could however be restrained within acceptable levels in all cases: the differences between the average WC sizes in the various samples (as determined by image analysis, Section 2.2) are indeed smaller than the experimental uncertainty (Table II).

The carbon loss of the HVOF-sprayed coatings (P2- and P3-series) is however perceivable through XRD patterns. The diffraction peaks of  $\text{W}_2\text{C}$  appear (Figure 3) and, at the same time, peaks of  $(\text{Co,Cr,W})_7\text{C}_3$  existing in the feedstock powder, as discussed in Section 3.1, disappear. The main diffraction peak of  $\text{W}_2\text{C}$ , located at  $2\theta \approx 39.94^\circ$ , is slightly shifted from the theoretical position ( $2\theta \approx 39.57^\circ$ , as listed in the JCPDF 35-776 file): in accordance with [22,54], this means that the  $\text{W}_2\text{C}$  phase contains some Cr, formed as a result of metallurgical interactions during the spray process. Namely, a  $(\text{W,Cr})_2\text{C}$  composition is formed: from the peak positions and from the corresponding lattice parameters, the Cr content, extrapolated from the graph given in [54] according to the procedure previously outlined in [51], is approximately 9 mol. %. This value is quite similar to the 6 mol. % content reported for an analogous HVOF-sprayed WC-10Co4Cr coating [51].



The HVAF-sprayed coatings (P1- and P4-series), by contrast, contain no detectable  $W_2C$  and retain the same phase composition of the corresponding feedstock powders (Figure 3), with peaks belonging to a f.c.c. Co-based solid solution and to the  $(Co,Cr,W)_7C_3$  carbide.

Diffraction peaks, however, are broader in the patterns of the HVAF-sprayed coatings than in the patterns of the powders (Figure 3), probably because of the extensive plastic deformation of the particles upon impact, so that the f.c.c.-Co phase peaks become nearly undetectable in the former.

Assuming the XRD technique has a detection threshold of about 2%, the index of WC retention is  $\geq 98\%$  for all HVAF-sprayed coatings, whereas the values for the HVOF-sprayed coatings was between 54% and 84% (Table II). Specifically, the coatings deposited using the finer feedstock powder (P2W1, P3W1) exhibit the lowest values of WC retention. Finer powder particles are proposed to be more thoroughly heated in the flame.

### 3.3 Mechanical properties

Hardness (Figure 5), indentation fracture toughness and elastic modulus (Figure 6A,B) data highlight important trends. On the one hand, whilst the two HVOF processes produce similar results, the M3-HVAF process produces harder, tougher coatings with higher elastic modulus than the M2-HVAF process, which may be due to differences in torch architectures, in fuel gases and in other process conditions (Section 2.1).

Specifically, elastic modulus values have very low data scatter, as testified by the standard deviation plotted as error bar in Figure 6B. The magnitude of the differences between the various samples can therefore be quantitatively evaluated by direct comparison of the average values. Indentation fracture toughness data is more scattered (Figure 6A); therefore, in order to understand which samples have a statistically meaningful difference, the Student's t-test is

needed. The average values of two data sets can be considered significantly different if the probability ( $p$ ) that the means are identical (i.e. the probability of the “null hypothesis”), computed through a paired-sample Student’s  $t$ -test or a two-sample  $t$ -test depending on whether the two data sets have different or identical variances (as determined through a preliminary  $F$ -test), is  $p < 0.05$ . The results, plotted in the table associated to Figure 6A, confirm that, for most of the pairs of P1-series and P4-series samples, the differences between the average  $K_{IC}$  values are indeed significant. Similar considerations hold for Vickers microhardness; the overall  $p$ -values table can be found in the supplementary data provided with the paper.

On the other hand, for each deposition process (P1-P4), the finer feedstock powder (W1-series) produces coatings with slightly higher toughness and elastic modulus than those obtained from the coarser one (W2-series). Once again, this is obvious for elastic modulus data, whilst the significance of the differences between pairs of  $K_{IC}$  values is confirmed by the Student’s  $t$ -test (Figure 6A). With each spray process, the finer powder therefore provides better interparticle cohesion. The finer powder particles probably exhibit better plastic flow behaviour upon impact onto the substrate. Particles therefore spread out more extensively, creating stronger interfaces with fewer defects.

It is also noted that the present indentation fracture toughness values of  $\approx 4 - 7 \text{ MPa}\cdot\text{m}^{1/2}$  (Figure 6) are consistent with literature values computed for similar WC-based coatings using the same equation [55-58].

Comparison of Vickers microhardness measurements at 300gf and 500 gf load (with the aid of the  $p$ -values from Student’s  $t$ -test provided in the supplementary data) also reveals a decrease from the W1-series to the W2-series sample, which is related to weaker long-range cohesive strength. Large material volumes, including a number of splats, are indeed affected at such indentation loads [59].

Microhardness at low loads, by contrast, is mainly affected by intra-lamellar properties; therefore, the significantly higher  $HV_{0.1}$  values of the HVOF-sprayed samples obtained from the fine feedstock powder (P2W1, P3W1) compared to those obtained from the coarse one (P2W2, P3W2) is probably related to the greater carbide dissolution observed in the former (Section 3.2 and Table II), which increases the hardness and brittleness of the matrix phase. Accordingly, the HVAF-sprayed samples, which never undergo measurable losses of WC phase (Section 3.2 and Table II), exhibit no significant change in  $HV_{0.1}$  values with coarsening of the feedstock powder (compare samples P1W1 to P1W2 and P4W1 to P4W2: Figure 5 and  $p$ -values table in the supplementary data).

As the test load increases, microhardness starts being somewhat affected by inter-lamellar cohesion as well. Stronger large-scale interlamellar cohesion in the samples obtained from the fine feedstock powder is therefore also proven by the fact that the distribution of hardness data in the W1-series samples becomes narrower with increasing indentation load (Figure 5A). In the coatings belonging to the W2-series, by contrast, the distribution of experimentally measured hardness values remains considerably broad from 100 gf to 500 gf (Figure 5B). This is mostly due to the presence of a comparatively higher amount of defects (resulting in increasing inter-lamellar sliding at higher loads) and to greater local variability (e.g. particles with different flattening and/or melting degrees) in the coatings of the W2-series, compared to the ones obtained from the finer powder W1.

### 3.4 Ball-on-disk testing

#### 3.4.1 Room temperature behaviour

At room temperature, the sliding wear rates of all WC-10Co4Cr coatings (Figure 7) are below  $10^{-7} \text{ mm}^3/(\text{Nm})$ , i.e. they correspond to a mild wear regime [60]. Under the present experimental conditions, they are orders of magnitude lower than those of electroplated hard

chromium references. The differences between the various WC-10Co4Cr coatings are small and often negligible within experimental error, as the probability of the “*null hypothesis*” from the Student’s t-test is  $p > 0.05$  for many of the data pairs (see the related table in Figure 7). Most of the statistically significant differences concern samples P2W1 and, particularly, P3W1. They indeed exhibit slightly higher wear rates than all other samples, which can be interpreted based on the following analysis of wear mechanisms.

The WC-10Co4Cr coatings exhibit a combination of two concurrent wear mechanisms:

- (i) Near-surface plastic deformation, leading to the formation of rough “waves” (Figure 8, label 1) consisting of lips of material extruded out of the surface (Figure 9C,D). Friction between the mating bodies induces a shear stress on the coating surface, directly on the contact area with the counterpart, which causes out-of-plane plastic flow of the metal matrix at an angle of approximately  $45^\circ$  with respect to the pristine surface plane. The WC grains, due to their fine size (micrometric and sub-micrometric, see Section 3.1), are dragged together with the matrix into these “wavy” extrusions. These “waves” have a micrometric length scale, hence the plastic flow phenomena probably occur at the intra-lamellar level.
- (ii) Brittle cracking, which leads to the detachment of small portions of material from the coating surface (Figure 8, label 2). This mechanism is probably mainly responsible for the largest part of the wear loss. The size of cracks and of the resulting voids left on the coating surfaces, ranging mostly from few micrometres to few tens of micrometres (Figure 9A,B), is usually smaller than the size of splats formed from the feedstock powder particles. Cracking during sliding contact, under the present test conditions, is therefore taking place at the intra-lamellar level, i.e. inside individual lamellae.

Both mechanisms occur simultaneously for all coatings: e.g., see Figures 9A and 9D showing two different details of the same worn surface. Their respective contributions to the wear loss, however, differ in the various samples. As they both take place at intra-lamellar level (which

is probably due to the small size of the contacting asperities on the mating bodies), their relative incidence is primarily determined by intra-lamellar properties. As a result, crack formation and propagation are more likely to occur on coatings which have been embrittled at the intra-lamellar scale by carbide dissolution and by carbon deficiency, such as samples P2W1 and P3W1 (see Section 3.2 and Table II). Coating properties at the inter-lamellar level (i.e. on a larger length scale) have comparatively lower relevance. This is supported by the fact that the wear rates of the coatings sprayed with the M2-HVAF process (P4W1, P4W2) are lower than those of samples P2W1 and P3W1 and comparable to those of all other WC-10Co4Cr coatings, although their inter-lamellar cohesion is poorer, as discussed in Section 3.3 based on hardness and toughness measurements (Figures 5 and 6).

These qualitative considerations are statistically supported by principal component analysis (PCA). The PCA method devises a set of  $n$  orthogonal vectors (the principal components), which represent a basis for the  $n$ -dimensional space constituted by a set of  $m$  measurements of  $n$  distinct variables. Of the infinite available orthogonal bases, PCA computes the one which best describes the variance of the data set. Namely, the first principal component accounts for the highest possible fraction of the overall variance of the data set, the second one accounts for the highest fraction of the remaining variance, etc. Each principal component is therefore a linear combination of the original variables.

In the present case, the selected variables are porosity and carbide content (from image analysis), index of carbide retention (from XRD peak fitting), Vickers microhardness measured with 100 gf ( $HV_{0.1}$ ) and 500 gf loads ( $HV_{0.5}$ ), indentation fracture toughness ( $K_{IC}$ ), elastic modulus ( $E$ ), and sliding wear rate at room temperature. They provide a  $(m = 8) \times (n = 8)$  matrix of experimental observations.

By applying the PCA method, a set of orthogonal principal components are devised, where the first and second ones alone account for about 80% of the variance of the data set (see the

Pareto chart in Figure 10A), whilst all components from the 5<sup>th</sup> to the 8<sup>th</sup> are basically insignificant. The following analysis will therefore focus on the first and second principal components only. The contributions of the original variables to these components are plotted as vectors in Figure 10B, together with the coordinates of each data point (i.e. of each of the eight WC-CoCr coatings) in the new reference system. The amount of carbides (measured both by the index of carbide retention and by the carbide content) and the microhardness at low load ( $HV_{0.1}$ ) are the variables which correlate best with the sliding wear rate.

The index of carbide retention and the sliding wear rate indeed provide nearly opposite contributions to the 1<sup>st</sup> and 2<sup>nd</sup> principal components, which means a decrease in carbide retention translates almost directly into an increase in sliding wear rate, in accordance with the previous discussion. Similar considerations hold for the carbide content, although carbide retention and carbide content are not coincident (Figure 10B), which probably comes from their different measurement methods (XRD peak fitting vs. image analysis).

Analogously, wear rate and  $HV_{0.1}$  have similar (though not identical) contributions to both of the principal components. It was accordingly observed in Section 3.3 that  $HV_{0.1}$  largely reflects intra-lamellar properties; in particular, it is affected by carbide dissolution. As the latter increases, the intra-lamellar material grows harder but it also loses toughness, thus becoming more prone to wear by micro-scale brittle fracture (as mentioned previously), resulting in higher wear rates as quantitatively shown by Figure 10B. The relation between the sliding wear rate and the  $HV_{0.5}$  value is less obvious, as the latter bears a greater influence from inter-lamellar cohesion (see Section 3.3), which has no significant role on sliding wear.

The wear rate is indeed almost orthogonal to the elastic modulus and to indentation fracture toughness. This leads to the following considerations:

- (i) The elastic modulus measured by the acoustic-wave propagation technique and the indentation fracture toughness obtained by high-load indentation testing are closely

related to one another as they both primarily measure large-scale interlamellar cohesion (as previously explained in Section 3.3);

- (ii) Inter-lamellar properties are not influential on the sliding wear behaviour, in accordance with the previous observations.

After plastic flow has occurred, the matrix is removed from the extruded lips, so that WC grains are soon protruding on top of the “waves”, as seen in Figures 9C,D. Following an initial running-in period, most of the contact is therefore borne by the WC grains alone. Due to their hardness, their tendency to stick to the alumina counterpart is low, so that no adhesion and no material transfer between the mating bodies occurs, consistent with the smooth and quite clean wear surface of the alumina counterpart (Figure 11A,B). The latter undergoes mild polishing wear at a rate of  $\leq 10^{-8} \text{ mm}^3/(\text{Nm})$ , lower than that of all WC-10Co4Cr coatings by up to one order of magnitude (in accordance with previous studies on similar material pairings [51,61]). The resulting friction coefficients are approximately 0.5 (Figure 7): they are not particularly low, but they indicate that no seizure occurs between the contacting surfaces.

As the wear loss of both the WC-10Co4Cr coatings and the counterpart is confined to a mild wear regime, very fine debris is produced, consisting of aggregates of nanometric particles (Figure 12A) with an amorphous structure, as seen in high resolution TEM micrographs and in the corresponding SAED patterns (Figure 12B). The Raman spectrum of this debris (Figure 13) is similar to that of amorphous Co/W oxides with high W content [62]. This Co-containing amorphous W oxide is formed by comminution and tribo-oxidation of very small fragments of coating material, coming either from the removal of the metal matrix together with a few WC grains during lip extrusion and “waves” formation (mechanism i), or from brittle cracking (mechanism ii). In [63], amorphous W-based oxide was also reported as the main constituent of the wear debris of bulk WC-Co in fretting contact against alumina. Very little Al is found in the debris (Figure 11C), as the wear loss of the  $\text{Al}_2\text{O}_3$  counterpart was previously shown to be one order of magnitude lower than that of the coating.

In the case of electrolytic hard chromium coatings, by contrast, more severe wear occurs by abrasion (Figure 14A) and adhesion (as indicated by the small delaminations seen in Figure 14B). Accordingly, the coating sticks to the counterbody and builds a transfer layer onto it (Figure 14C), resulting in much higher friction coefficient than that produced by WC-10Co4Cr under the same experimental conditions (Figure 7). Debris particles are also much bigger (Figure 15A). They are partly crystalline (Figure 15B and SAED pattern in Figure 15C) and, based on the low intensity of the oxygen peak in the corresponding EDX spectra (Figure 16A – note that this peak is also partly overlapped by the Cr-L lines), they are probably not completely oxidised, i.e. they contain quite coarse fragments of chromium. The presence of an oxidised fraction is however indicated by the possibility to acquire well-defined Raman spectra (Figure 16B). Straightforward interpretation of these spectra is not easy: the broad feature at  $\approx 550\text{ cm}^{-1}$  can be ascribed to Cr(III) oxi-hydroxides [64], but the main peak at  $\approx 880\text{ cm}^{-1}$  may belong either to chromate species [64] or to  $\text{Cr}_2\text{O}_3$  nanoparticles with hydroxylated surfaces [65]. The possible release of chromates in the debris, as a result of wear and tribo-oxidation of electroplated hard chromium in sliding contacts, has not been examined in the literature up to now, and it cannot be undoubtedly claimed based on the present results. Deeper investigation on this topic is outside the aim of this work, but it should be carried out in future research. If the finding of Cr(VI) in the debris is confirmed, indeed, it would constitute another important health and safety issue calling for the replacement of electroplated hard chromium.

### 3.4.2 Behaviour at 400 °C

At 400 °C, the wear rates of WC-10Co4Cr coatings increase by one order of magnitude and become somewhat higher than  $10^{-7}\text{ mm}^3/(\text{Nm})$  (Figure 7), with the exception of samples P3W1 and P3W2, which failed due to the development of a macroscopically visible network



of through-thickness cracks across their entire surface (Figure 17). The cracks, which propagate with a somewhat tortuous path across the coating, often reaching down to the substrate (Figure 18B), were probably formed as the sample reached the test temperature, before the sliding test was commenced, so that ball and sample wear rates are not meaningful in this case.

#### 3.4.2.1 Analysis of crack formation

The formation of cracks in the samples deposited by the P3 process (namely, Diamond Jet 2700 HVOF spraying) is probably due to a number of superimposed factors, including (a) precipitation of secondary carbides, (b) development of thermal expansion mismatch stresses and (c) presence of residual stresses, as explained below.

(a) The microstructure of the HVAF-sprayed samples does not change after high-temperature exposure (Figure 18A,C). In the HVOF-sprayed coatings, on the other hand, few secondary bright (W-rich) phases appear in the form small, irregularly-shaped precipitates, often located around some of the original WC grains (see circled areas in Figure 18D). Most probably, W-based secondary carbides precipitated from the matrix, which contained W and C because of the dissolution of WC during HVOF-spraying, as discussed in Section 3.2. Such precipitation has accordingly been observed in some previous works, though at somewhat higher temperatures [66,67]. This phenomenon alone, however, cannot account for the appearance of cracks, which affects only the samples deposited with one of the two HVOF processes.

(b) In the temperature range from 30 °C to 400 °C, the thermal expansion coefficient of WC-10Co4Cr is less than half of that of the substrate (Table III). The experimentally measured CTE values listed in Table III are qualitatively in a good agreement with those measured for HVOF-sprayed WC – 17 wt.% Co by Thiele et al. [42]. As the sample reaches

the test temperature of 400 °C, the coating becomes subject to significant tensile stresses, an analytical estimate of which can be obtained using the composite beam theory as laid out e.g. in [68]. Specifically, two opposite normal forces ( $F_T$ ) act on the coating and on the substrate due to thermal expansion mismatch (Figure 19), and a bending moment ( $M_T$ ) arises to balance the normal forces torque. The thermal expansion mismatch stresses on top of the coating layer ( $\sigma_{y=h}^T$ ) and at the coating-substrate interface ( $\sigma_{y=0}^T$ ) are therefore computed as the sum of the contributions due to the normal force and to the bending moment:

$$\sigma_{y=h}^T = \frac{F_T}{bh} - E_C \kappa (h - \delta) \quad (3.1)$$

$$\sigma_{y=0}^T = \frac{F_T}{bh} - E_C \kappa \delta \quad (3.2)$$

With:  $\delta = \frac{E_C h^2 - E_S H^2}{2(E_C h + E_S H)}$  = neutral axis position

$\kappa = M_T / \Sigma$  = curvature of the coated system

$\Sigma = bhE_C \left( \frac{h^2}{3} - h\delta + \delta^2 \right) + bHE_S \left( \frac{H^2}{3} + H\delta + \delta^2 \right)$  = flexural stiffness

$M_T = F_T \frac{H+h}{2}$  = bending moment

$F_T = b(\alpha_S - \alpha_C)\Delta T \frac{HhE_SE_C}{hE_C + HE_S}$  = normal force

With reference to the diagram in Figure 19:  $b$  = out-of-plane sample width (= 50 mm);  $h$  = coating thickness ( $\approx 0.35$  mm, see Section 2.1);  $H$  = substrate thickness (= 8 mm);  $\Delta T$  = temperature change = (400 – 20) °C = 380 °C;  $\alpha_S$ ,  $\alpha_C$  = thermal expansion coefficients of the substrate and of the coating (from Table III).

The elastic modulus of the steel substrate is  $E_S = 210$  GPa, whereas that of HVOF-sprayed WC-10Co4Cr coatings ( $E_C$ ), as shown in Figure 5B, is approximately comprised in the 250 – 300 GPa range; therefore, from equations (3) it follows:  $\sigma_{y=h}^T = 566 - 654$  MPa,  $\sigma_{y=0}^T = 574 - 665$  MPa.

Since the thermal expansion coefficient is not strongly dependent on the microstructure of a coating, it can be quite confidently assumed that the values in Table III and, therefore, the

above thermal stress estimates are representative of all WC-10Co4Cr coatings employed in this study.

(c) As the crack network only affects the samples deposited by the Diamond Jet HVOF process, the thermal expansion mismatch is not its only cause. Notably, in a previous study [28], other WC-10Co4Cr coatings sprayed by Diamond Jet 2600 process, using hydrogen as fuel gas, onto carbon steel developed an analogous macro-crack network upon heating to 500 °C. The systematic recurrence of the phenomenon in coatings deposited by this specific process suggests the occurrence of some additional deposition-related factor. Decarburisation during spraying and consequent high-temperature precipitation of secondary phases during testing is also not a viable explanation, as discussed in point a). The cause more reasonably lies in the residual stress state of the coatings.

X-ray residual stress analysis was therefore performed on the samples deposited with fine powder feedstock (W1 series). The results (Table IV) clearly show that, compared to the other coatings, sample P3W1 is subject to significantly higher tensile residual stresses on its top surface. Overall stress levels as high as 900 – 1000 MPa in the samples deposited by the Diamond Jet HVOF process can therefore result from the superposition of their residual stresses, listed in Table IV, with thermal expansion mismatch stresses previously estimated at point (b). Such stress levels are obviously capable of inducing extensive cracking of the P3-series coatings.

The JP5000-HVOF sprayed coating (sample P2W1) is subjected to comparatively lower tensile residual stresses on its top surface: this is probably due to the higher impact velocity of particles sprayed by liquid-fuelled HVOF processes, inducing greater peening effects which partly balance the tensile quenching stress contribution [69].

In the HVAF process, stronger peening effects and less splat quenching result in almost zero residual stress on the top surface. The stress values of samples P1W1 and P4W1 as listed in

Table V are indeed almost of the same order of magnitude of the accuracy of the X-ray residual stress measurement technique, which is usually of  $\approx 20$  MPa.

### 3.4.2.2 Analysis of wear mechanisms

All non-failed samples (P1, P2 and P4 series) have quite similar wear rates at 400 °C; indeed, only few of the  $p$ -values from Student's  $t$ -test are below the statistical significance threshold of 0.05, and almost none falls below 0.01 (see the related table in Figure 7). Accordingly, all of their wear mechanisms are substantially similar, and they differ remarkably from those appearing at room temperature (Section 3.4.1). This is consistent with the previously reported order-of-magnitude increase in wear rates (Figure 7). Specifically, the wear scars bear evidence of more severe abrasive grooving (Figure 20A), affecting the WC grains as well (Figure 20B,C).

The hardness of WC is reported to be nearly constant in the temperature range up to 400 °C [70,71]. However, SEM micrographs (Figure 21A) and AFM maps (Figure 21B) acquired outside the wear scar show that WC grains not covered with the metallic binder developed oxide protrusions consisting of  $WO_3$  (see Raman spectrum in Figure 21C), whilst the matrix remained relatively unaffected. Due to its specific volume being much larger than that of WC,  $WO_3$  adheres poorly to the underlying carbide grain and grows with significant defects [72], so it is expected to be easily removed during sliding. Permanent removal of the  $WO_3$  scale and ongoing fast oxidation of WC grains are therefore plausible causes for the observed abrasive grooving.

The carbide grains therefore become unable to prevent the coating from sticking to the alumina counterbody. Evidence of adhesive wear is indeed found, with material being torn out of the coating surface (Figure 20D), and a transfer layer is built up on the counterpart (Figure 22). Adhesive wear and the consequent onset of self-mated contact between the coating and

the transfer layer account for the high friction coefficient recorded at this temperature (usually around 1, Figure 7).

Friction induces tensile stresses on the coating surface, behind the contact region: the coupling of this stress to the thermal expansion mismatch stress discussed in Section 3.4.2.1 results in transverse microcracking across the entire wear scar (Figure 20B,C: see arrows). Consistent observations were reported by the authors in a previous study [29]. Such cracks were not found in the wear scars of HVOF-sprayed WC-FeCrAl coatings tested at the same temperature in that study [29], in spite of its thermal expansion coefficient [29] being practically identical to that of the present WC-10Co4Cr samples. This indicates that some form of high-temperature brittleness also contributes to making WC-10Co4Cr unable to withstand the combined action of these stresses.

### 3.5 *Dry sand-rubber wheel testing*

Volume losses after dry sand-rubber wheel testing were computed from mass losses using the density values listed in Table II, as described in Section 2.3. The ranking of the various WC-10Co4Cr coatings in this test (Figure 23) is different from sliding wear conditions at room temperature and clearly depends on the feedstock powder particle size. Namely, the coatings obtained from the coarse feedstock powder (W2-series) experience somewhat larger volume losses than those obtained from the fine powder (W1-series).

The factors underlying this behaviour can be interpreted with the aid of PCA results. In addition to the abrasive volume loss (Figure 23), the chosen variables, as in Section 3.4.1, are porosity, carbide content, index of carbide retention (Table II),  $HV_{0.1}$ ,  $HV_{0.5}$  (Figure 5), elastic modulus and  $K_{IC}$  (Figure 6). Once again, focus can be placed on the first and second principal components only, as they jointly account for around 80% of the overall variance (Pareto chart in Figure 24A). The contributions of the different variables to such components (Figure 24B)

depict a completely opposite situation, as compared to the sliding wear results in Section 3.4.1. The abrasive volume loss is poorly related or even almost orthogonal (i.e. unrelated) to the variables (index of carbide retention, carbide content,  $HV_{0.1}$ ) which were the most influential on the sliding wear rate. Instead, it is closely connected to parameters which measure long-range interlamellar cohesion (elastic modulus and indentation fracture toughness) and microstructural defectiveness (porosity).

It is therefore concluded that intra-lamellar properties, which controlled the sliding wear behaviour, are largely irrelevant for the abrasive wear resistance. The latter benefits the most from high coating density and strong interlamellar cohesion.

This behaviour is explained by the two main wear mechanisms controlling the dry particle abrasion of these materials, identified by SEM micrographs of the wear scars (representative overviews in Figure 25A,B). On one hand, the binder matrix is abraded until the unsupported WC grains are cracked and pulled out of the surface, as observed e.g. in Figure 25C. On the other hand, larger portions of material are detached from the surface by brittle fracture (see circled areas in Figure 25A,B; detail in Figure 25D). Similar mechanisms of matrix abrasion and brittle fracture were also reported in various previous studies [30,73-75]. Brittle fracture, which is clearly responsible for the greater part of the wear loss, appears more frequently for coatings deposited from the coarse feedstock powders (compare Figure 25B to Figure 25A).

The size of these delaminated regions, ranging from some tens of micrometres up to  $\approx 100$  micrometres, matches with the expected size of lamellae obtained by deformation and flattening of the impacting feedstock powder particles. It is therefore inferred that brittle removal of entire lamellae is taking place (as previously reported in [75]); namely, the resistance to dry particle abrasion largely depends on inter-lamellar cohesion, differently from ball-on-disk dry sliding wear (which is primarily controlled by intra-lamellar features such as carbide dissolution and carbon deficiency, Section 3.4.1) and consistently with the previous

PCA results (Figure 24). The abrasive grits employed in the rubber wheel test are indeed much larger than the surface asperities coming in contact under dry sliding conditions. When they are pressed against the coating surface, they can stress many lamellae at the same time and cause the detachment of the most weakly bonded ones. This phenomenon therefore occurs more frequently in coatings obtained from the coarse feedstock powder (W2-series) on account of their poorer inter-lamellar bonding, previously inferred from porosity (Section 3.2), modulus and fracture toughness (Section 3.3) measurements.

#### 4 Conclusions

The systematic investigations performed in this study, including the characterisation of the tribological properties of HVOF- and HVAF-sprayed WC-10Co4Cr coatings under sliding and abrasive wear conditions, and the related statistical analyses of the resulting data lead to the following conclusions:

- Different from other types of carbon-deficient sintered and crushed feedstock powders [22], the one used in this study exhibits a carbon content above the nominal value. This leads to the formation of  $(\text{Co,Cr,W})_7\text{C}_3$  which exists as large grains in the powder and is found in the HVAF coatings as well, due to low carbon loss in this process. It is not found in the HVOF coatings due to more intensive metallurgical reactions and higher carbon loss.
- All HVOF- and HVAF-spray processes used in this study are capable of producing dense WC-10Co4Cr coatings. The former cause higher carbon loss, and thus lower WC content in the coatings. In all deposition processes, the finer feedstock powder produces denser and harder coatings, with higher indentation fracture toughness and higher elastic modulus than the coarse one.

- At room temperature, the dry sliding wear behaviour of WC-10Co4Cr coatings is dominated by two concurrent mechanisms: ductile flow, which causes the formation of “wavy” lips with protruding WC grains, and brittle fracture, which causes direct detachment of small portions of material from the coating surface.  
The relative incidence of the two mechanisms is mainly controlled by intra-lamellar features, such as decarburisation. This is probably related to the small size of the contacting asperities, which matches with the intra-lamellar length scale. HVOF-sprayed coatings obtained from fine feedstock powders, being somewhat more decarburised, therefore suffer slightly higher wear loss due to the increased incidence of brittle fracture phenomena.  
In all cases, anyway, both the coatings and the alumina counterpart are in a mild wear regime. Friction coefficients are roughly around 0.5, with no adhesion between the mating bodies. The nanometric size of the wear debris is also consistent with very mild wear process.
- At 400 °C, WC grains at the coating surface are oxidised to  $WO_3$ . More severe abrasive grooving takes place, and adhesion to the counterpart also occurs. Wear rates increase by one order of magnitude and the friction coefficient is roughly doubled to  $\approx 1$ .
- At 400 °C, tensile stresses due to thermal expansion mismatch with the substrate can sometimes cause complete failure of the coating by brittle cracking, if they are coupled to pre-existing tensile residual stresses after deposition. Spraying processes capable of inducing lower residual stresses are therefore favoured in this case, as they can restrain or prevent this phenomenon. In any case, cracking across the wear scar is observed even in non-failed samples, indicating a dangerously high tensile stress level in all coatings.
- The dry particle abrasion behaviour is mainly controlled by inter-lamellar cohesion. Coatings obtained from coarse feedstock powders have weaker cohesion, which is also witnessed by lower elastic modulus, lower indentation fracture toughness and higher



porosity compared to the corresponding coatings obtained from fine feedstock powders, and therefore suffer more severe abrasive wear due to the increased incidence of inter-lamellar detachment phenomena.

- It is concluded that both HVOF- and HVAF-spraying processes are able to produce coatings with satisfactory tribological properties, which are deemed to be suitable for industrial applications. The selection of the deposition process and of the feedstock powder should be made depending on the specific application, as distinct tribological conditions may probe different coating properties, as shown above.
- At room temperature, under both abrasive and sliding wear conditions, all of the tested WC-10Co4Cr coatings are more wear resistant than reference electroplated hard chromium.

**Acknowledgements**

Many thanks to Dr. Benno Gries, Dr. Stefan Zimmermann and Dr. Olav Norheim (H.C. Starck GmbH, Laufenburg, Germany) for providing the feedstock powders and the JP5000-HVOF sprayed coatings for this research, and to Mr. Moreno Ghiaroni (Galvanica Nobili s.r.l., Marano Sul Panaro (MO), Italy) for providing hard chromium electroplated samples.

The authors are grateful to Ing. Chiara Venturelli (Expert System Solutions s.r.l., Modena, Italy) for optical dilatometer tests and to Dr. Mauro Zapparoli (University of Modena and Reggio Emilia) for assistance with TEM observations. In addition, the authors express thanks to Mr. Roberto Puschmann for spraying samples at Fraunhofer IWS and to Mr. Andrea Milanti (Tampere University of Technology, Tampere, Finland) for XRD measurements.

## References

- [1] M. Li, P.D. Christofides, Multi-scale modeling and analysis of an industrial HVOF thermal spray process, *Chem. Eng. Sci.* 60 (2005) 3649-3669.
- [2] J.R. Davis (Ed.), *Handbook of Thermal Spray Technology*, ASM International, Materials Park, OH, USA, 2004.
- [3] B.D. Sartwell, K.O. Legg, J. Zimmerman, M. Reynolds, A. Drennan, J. Gribble, J. Magno, R. Mason, A. Kaltenhauser, Validation of HVOF Thermal Spray Coatings as a Replacement for Hard Chrome Plating on Hydraulic/Pneumatic Actuators, Naval Research Laboratory Final Report, 27-07-2006.
- [4] K.O. Legg, M. Graham, P. Chang, F. Rastagar, A. Gonzales, B. Sartwell, The replacement of electroplating, *Surf. Coat. Technol.* 81 (1996) 99-105.
- [5] G. Montavon, A. Vardelle, N. Krishnan, P. Ulloa, S. Costil, H. Liao, Life Cycle Assessment (LCA) of Thermal-Sprayed and Chromium Electroplated Coatings, in: B. R. Marple, M.M. Hyland, Y.-C. Lau, R.S. Lima, J. Voyer (Eds.), *Building on 100 Years of Success: Proceedings of the International Thermal Spray Conference 2006*, ASM International, Materials Park, OH, USA, 2006.
- [6] U.S. Department of Labor, Occupational Safety and Health Administration, Hexavalent Chromium, Report 3373-10, 2009. Available on-line at: <https://www.osha.gov/Publications/OSHA-3373-hexavalent-chromium.pdf>
- [7] EU Commission Regulation No 348/2013 amending Annex XIV to Regulation (EC) No 1907/2006 of the European Parliament and of the Council on the Registration, Evaluation, Authorisation and Restriction of Chemicals (REACH), *Official Journal of the European Union*, 18.4.2013, L108/1 – L108/5.
- [8] R. Schwetzke, H. Kreye, Microstructure and properties of tungsten carbide coatings sprayed with various high-velocity oxygen fuel spray systems, *J. Therm. Spray Technol.* 8(3) (1999) 433-439.
- [9] H.M. Hawthorne, B. Arsenault, J.P. Immarigeon, J.G. Legoux, V.R. Parameswaran, Comparison of slurry and dry erosion behaviour of some HVOF thermal sprayed coatings, *Wear* 225–229 (1999) 825–834.
- [10] C. Bartuli, T. Valente, F. Cipri, E. Bemporad, M. Tului, Parametric study of an HVOF process for the deposition of nanostructured WC-Co coatings, *J. Therm. Spray Technol.* 14(2) (2005) 187-195.
- [11] Q. Wang, S. Zhang, Y. Cheng, J. Xiang, X. Zhao, G. Yang, Wear and corrosion performance of WC-10Co4Cr coatings deposited by different HVOF and HVAF spraying processes, *Surf. Coat. Technol.* 218 (2013) 127–136.
- [12] L.-M. Berger, Coatings by Thermal Spray, in: V. Sarin (ed-in-chief), D. Mari, L. Llanes (vol. eds.), *Comprehensive Hard Materials – Vol. 1: Hardmetals*, Elsevier, Amsterdam, The Netherlands, 2014, p.471-506.

- [13] A. Wank, A. Schwenk, B. Wielage, T. Grund, E. Friesen, H. Pokhmurska, Untersuchungen zur Beständigkeit thermisch gespritzter Schichten im Vergleich zu Hartchromschichten bei durch Abrasion dominierter tribologischer Beanspruchung (Investigations on thermal spray coatings resistance against abrasion dominated tribological load in comparison to hard chromium coatings), *Materialwiss. Werkstofftech.* 38(2) (2007) 144-148 (in German).
- [14] S. Kamnis, S. Gu, T.J. Lu, C. Chen, Computational simulation of thermally sprayed WC-Co powder, *Comput. Mater. Sci.* 43 (2008) 1172-1182.
- [15] J. Berget, T. Rogne, E. Bardal, Erosion-corrosion properties of different WC-Co-Cr coatings deposited by the HVOF process—influence of metallic matrix composition and spray powder size distribution, *Surf. Coat. Technol.* 201 (2007) 7619-7625.
- [16] D.A. Stewart, P.H. Shipway, D.G. McCartney, Abrasive wear behaviour of conventional and nanocomposite HVOF-sprayed WC-Co coatings, *Wear* 225-229 Part 2 (1999) 789-798.
- [17] P.H. Shipway, D.G. McCartney, T. Sudaprasert, Sliding wear behaviour of conventional and nanostructured HVOF sprayed WC-Co coatings, *Wear* 259(7-12) (2005) 820-827.
- [18] S. Usmani, S. Sampath, D.L. Houck, D. Lee, Effect of Carbide Grain Size on the Sliding and Abrasive Wear Behavior of Thermally Sprayed WC-Co Coatings, *Tribol. Trans.* 40(3) (1997) 470-478.
- [19] C. Verdon, A. Karimi, J.-L. Martin, Microstructural and analytical study of thermally sprayed WC-Co coatings in connection with their wear resistance, *Mater. Sci. Eng. A* 234-236 (1997) 731-734.
- [20] L.-M. Berger, R. Puschmann, J. Spatzier, S. Matthews, Potential of HVAF spray processes. *Therm. Spray Bull.* 6(1) (2013) 16-20.
- [21] L.-M. Berger, P. Vuoristo, T. Mäntylä, W. Kunert, W. Lengauer, P. Ettmayer, Microstructure and Properties of WC-Co-Cr Coatings, in: C.C. Berndt (Ed.), *Thermal Spray: Practical Solutions for Engineering Problems – Proceedings of the 9th National Thermal Spray Conference*, ASM International, Materials Park, OH, USA, 1996, pp. 97-106.
- [22] L.-M. Berger, P. Ettmayer, P. Vuoristo, T. Mäntylä, W. Kunert, Microstructure and properties of WC-10%Co-4% Cr spray powders and coatings: Part 1. Powder characterization, *J. Therm. Spray Technol.* 10(2) (2001) 311-325.
- [23] K. Frisk, A. Markström, Effect of Cr and V on Phase Equilibria in Co-WC Based Hardmetals, *Int. J. Mater. Res.* 99(3) (2008) 287-293.
- [24] B. Gries, S. Zimmermann, Corrosion behaviour of HVOF sprayed carbide coatings, in: *Proceedings of the 9th HVOF Kolloquium, Gemeinschaft Thermisches Spritzen eV, Unterschleißheim, Germany, 2012*, pp. 71-78.
- [25] M. Magnani, P.H. Suegama, N. Espallargas, S. Dosta, C.S. Fugivara, J.M. Guilemany, A.V. Benedetti, Influence of HVOF parameters on the corrosion and wear resistance of WC-Co coatings sprayed on AA7050 T7, *Surf. Coat. Technol.* 202 (2008) 4746-4757.

- [26] Q. Wang, Z. Chen, L. Li, G. Yang, The parameters optimization and abrasion wear mechanism of liquid fuel HVOF sprayed bimodal WC–12Co coating, *Surf. Coat. Technol.* 206 (2012) 2233–2241.
- [27] S. Houdková, M. Kašparová, F. Zahálka, The friction properties of HVOF sprayed hardmetal coatings, in: *Proceedings of the 19<sup>th</sup> International Conference on Metallurgy and Materials*, 18-20 May 2010, Czech Republic. Available on-line at: [http://www.metal2014.com/files/proceedings/metal\\_10/lists/papers/34.pdf](http://www.metal2014.com/files/proceedings/metal_10/lists/papers/34.pdf)
- [28] E. Bergonzini, G. Bolelli, B. Bonferroni, L. Lusvarghi, T. Varis, U. Kanerva, T. Suhonen, J. Oksanen, O. Söderberg, S.-P. Hannula, Wear behaviour of HVOF-sprayed nanostructured WC-CoCr coatings, in: B.R. Marple, A. Agarwal, M.M. Hyland, Y.-C. Lau, C.-J. Li, R.S. Lima, A. McDonald (eds.), *Thermal Spray 2011: Proceedings of the International Thermal Spray Conference*, DVS-Verlag, Düsseldorf, Germany, 2011, pp. 23–34.
- [29] G. Bolelli, I. Hulka, H. Koivuluoto, L. Lusvarghi, A. Milanti, K. Niemi, P. Vuoristo, Properties of WC-FeCrAl coatings manufactured by different high velocity thermal spray processes, submitted to *Surf. Coat. Technol.*
- [30] Y. Qiao, Y.R. Liu, T.E. Fischer, Sliding and Abrasive Wear Resistance of Thermal-Sprayed WC-Co Coatings, *J. Therm. Spray Technol.* 10(1) (2001) 118-125.
- [31] J.A. Picas, M. Punset, M.T. Baile, E. Martín, A. Forn, Tribological evaluation of HVOF thermal-spray coatings as a hard chrome replacement, *Surf. Interface Anal.* 43 (2011) 1346-1353.
- [32] I. Hulka, V.-A. Șerban, K. Niemi, P. Vuoristo, J. Wolf, Comparison of structure and wear properties of fine-structured WC-CoCr coatings deposited by HVOF and HVOF spraying processes, *Diffus. Defect Data Part B: Solid State Phenom.* 188 (2012) 422-427.
- [33] L. Jacobs, M.M. Hyland, M. De Bonte, Study of the Influence of Microstructural Properties on the Sliding-Wear Behavior of HVOF and HVOF Sprayed WC-Cermet Coatings, *J. Therm. Spray Technol.* 8(1) (1999) 125-132.
- [34] L. Jacobs, M.M. Hyland, M. De Bonte, Comparative Study of WC-Cermet Coatings Sprayed via the HVOF and the HVOF Process, *J. Therm. Spray Technol.* 7(2) (1998) 213-218.
- [35] L.-M. Berger, M. Woydt, S. Saaro, Comparison of self-mated hardmetal coatings under dry sliding conditions up to 600 °C, *Wear* 266 (2009) 406–416.
- [36] Q. Yang, T. Senda, A. Hirose, Sliding wear behavior of WC–12% Co coatings at elevated temperatures, *Surf. Coat. Technol.* 200 (2006) 4208–4212.
- [37] M. Abramoff, P. Magalhães, S. Ram, Image Processing with ImageJ, *Biophotonics Int.* 11(7) (2004) 36–42.
- [38] M.M. Lima, C. Godoy, P.J. Modenesi, J.C. Avelar-Batista, A. Davison, A. Matthews, Coating fracture toughness determined by Vickers indentation: an important parameter in

cavitation erosion resistance of WC–Co thermally sprayed coatings, *Surf. Coat. Technol.* 177–178 (2004) 489–496.

[39] K. Niihara, R. Morena, D.P.H. Hasselman, Evaluation of  $K_{Ic}$  of brittle solids by the indentation method with low crack-to-indent ratios, *J. Mater. Sci. Lett.* 1 (1982) 13–16.

[40] L.-M. Berger, D. Schneider, M. Barbosa, R. Puschmann, Laser Acoustic Surface Waves for the Non-Destructive Characterisation of Thermally Sprayed Coatings, *Therm. Spray Bull.* 5(1) (2012) 56–64.

[41] L.-M. Berger, D. Schneider, T. Großer, Non-destructive testing of coatings by surface acoustic waves, in: B.R. Marple, M.M. Hyland, Y.-C. Lau, C.-J. Li, R.S. Lima, G. Montavon (Eds.), *Global Coating Solutions – Proceedings of the 2007 International Thermal Spray Conference*, ASM International, Materials Park, OH, USA, 2007, pp. 916–921 (CD).

[42] S. Thiele, K. Sempf, K. Jaenicke-Roessler, L.-M. Berger, J. Spatzier, Thermophysical and Microstructural Studies on Thermally Sprayed Tungsten Carbide-Cobalt Coatings, *J. Therm. Spray Technol.* 20(1-2) (2011) 358–365.

[43] [www.matweb.com](http://www.matweb.com) (last accessed 17/02/2014)

[44] P. Niranatlumpong, C. Sukhonket, J. Nakngonthong, Wear resistant surface treatment of pulverizer blades, *Wear* 302 (2013) 878–881.

[45] A.C. Vermeulen, The sensitivity of focusing, parallel beam and mixed optics to alignment errors in XRD residual stress measurements, *Mater. Sci. Forum* 490-491 (2005) 131-136.

[46] A.C. Vermeulen, D. Götz, Data collection requirements for the analysis of residual stress in polycrystalline coatings, *Mater. Sci. Forum* 524-525 (2006) 793-800.

[47] U. Welzel, J. Ligot, P. Lamparter, A.C. Vermeulen, E.J. Mittemeijer, Stress analysis of polycrystalline thin films and surface regions by X-ray diffraction, *J. Appl. Crystall.* 38 (2005) 1-29.

[48] B. Eigenmann, Röntgenographische Untersuchung von Spannungszuständen in Werkstoffen. Teil III, *Mater.-wiss. Werkstofftech.* 27(9) (1996) 426–437 (in German).

[49] A. Portinha, V. Teixeira, J. Carneiro, M.G. Beghi, C.E. Bottani, N. Franco, R. Vassen, D. Stoeber, A.D. Sequeira, Residual stresses and elastic modulus of thermal barrier coatings graded in porosity, *Surf. Coat. Technol.* 188–189 (2004) 120–128.

[50] J. Zackrisson, B. Jansson, G.S. Upadhyaya, H.-O. Andrén: WC-Co Based Cemented Carbides with Larger  $Cr_3C_2$  Additions, *Int. J. Refract. Met. Hard Mater.* 16(4-6) (1998) 417-422.

[51] G. Bolelli, L.-M. Berger, M. Bonetti, L. Lusvarghi, Comparative study of the dry sliding wear behaviour of HVOF-sprayed WC–(W,Cr)<sub>2</sub>C–Ni and WC–CoCr hardmetal coatings, *Wear* 309 (2014) 96–111.

[52] P. Vuoristo, Thermal Spray Coating Processes. In: D. Cameron (Ed.), *Comprehensive Materials Processing – Vol. 4*, Elsevier, Amsterdam, The Netherlands, 2014, pp. 229-276.

- [53] T. Varis, T. Suhonen, A. Ghabchi, A. Valarezo, S. Sampath, X. Liu, S.-P. Hannula, Formation Mechanisms, Structure, and Properties of HVOF-Sprayed WC-CoCr Coatings: An Approach Toward Process Maps, *J. Therm. Spray Technol.* 23(6) (2014) 1009–1018.
- [54] P. Stecher, F. Benesovsky, H. Nowotny, Untersuchungen im System Chrom-Wolfram-Kohlenstoff, *Planseeber. Pulvermet.* 12(2) (1964) 89-95 (in German).
- [55] M.M. Lima, C. Godoy, J.C. Avelar-Batista, P.J. Modenesi, Toughness evaluation of HVOF WC–Co coatings using non-linear regression analysis, *Mater. Sci. Eng. A* 357(1–2) (2003) 337–345.
- [56] Š. Houdková, M. Kašparová, Experimental study of indentation fracture toughness in HVOF sprayed hardmetal coatings, *Eng. Fract. Mech.* 110 (2013) 468–476.
- [57] M. Xie, S. Zhang, M. Li, Comparative investigation on HVOF sprayed carbide-based coatings, *Appl. Surf. Sci.* 273 (2013) 799–805.
- [58] Q. Wang, Z. Chen, L. Li, G. Yang, The parameters optimization and abrasion wear mechanism of liquid fuel HVOF sprayed bimodal WC–12Co coating, *Surf. Coat. Technol.* 206(8–9) (2012) 2233–2241.
- [59] J. Nohava, B. Bonferroni, G. Bolelli, L. Lusvarghi, Interesting aspects of indentation and scratch methods for characterization of thermally-sprayed coatings, *Surf. Coat. Technol.* 205(4) (2010) 1127-1131.
- [60] K. Kato, K. Adachi, Wear of advanced ceramics, *Wear* 253 (2002) 1097-1104.
- [61] L.-M. Berger, M. Woydt, S. Saaro, Reib-/Gleitverschleiß von thermisch gespritzten Hartmetallschichten, *Jahrbuch Oberflächentechnik* (ed. R. Suchentrunk), Vol. 63, Bad Saulgau, Eugen G. Leuze Verlag, 2007, 242–267.
- [62] J.E. Herrera, D.E. Resasco, Role of Co-W Interaction in the Selective Growth of Single-Walled Carbon Nanotubes from CO Disproportionation, *J. Phys. Chem. B* 107 (2003) 3738-3746.
- [63] H. Mohrbacher, B. Blanplain, J.-P. Celis, J.R. Roos, Raman spectroscopy on defective wear debris generated by contact vibrations, *J. Mater. Sci. Lett.* 14 (1995) 279-281.
- [64] J.E. Maslar, W.S. Hurst, W.J. Bowers Jr., J.H. Hendricks, M.I. Aquino, I. Levin, In situ Raman spectroscopic investigation of chromium surfaces under hydrothermal conditions, *Appl. Surf. Sci.* 180(1–2) (2001) 102-118.
- [65] J. Yang, H. Cheng, W.N. Martens, R.L. Frost, Transition of synthetic chromium oxide gel to crystalline chromium oxide: a hot-stage Raman spectroscopic study, *J. Raman Spectrosc.* 42 (2011) 1069–1074.
- [66] Sh. Khameneh Asl, M. Heydarzadeh Sohi, K. Hokamotoa, M. Uemura, Effect of heat treatment on wear behavior of HVOF thermally sprayed WC-Co coatings, *Wear* 260 (2006) 1203–1208.
- [67] Q. Wang, L. Li, G. Yang, X. Zhao, Z. Ding, Influence of heat treatment on the microstructure and performance of high-velocity oxy-fuel sprayed WC–12Co coatings, *Surf. Coat. Technol.* 206 (2012) 4000–4010.

- [68] Y.C. Tsui, T.W. Clyne, An analytical model for predicting residual stresses in progressively deposited coatings. Part I: Planar geometry, *Thin Solid Films* 306 (1997) 23-33.
- [69] G. Bolelli, V. Cannillo, L. Lusvarghi, R. Rosa, A. Valarezo, W.B. Choi, R. Dey, C. Weyant, S. Sampath, Functionally graded WC–Co/NiAl HVOF coatings for damage tolerance, wear and corrosion protection, *Surf. Coat. Technol.* 206(8–9) (2012) 2585–2601.
- [70] L.E. Toth, *Transition Metal Carbides and Nitrides*, Academic Press, New York and London, 1971, pp. 176-184.
- [71] A.S. Kurllov, A.I. Gusev, *Tungsten Carbides. Structure, Properties and Application in Hardmetals – Springer Series in Materials Science Vol. 184*, Springer, Heidelberg, Germany, 2013, pp. 34-36.
- [72] S.N. Basu, V.K. Sarin, Oxidation behavior of WC-Co, *Mater. Sci. Eng. A* 209 (1996) 206-212.
- [73] Y. Liu, Y. Qiao, J. He, E. Lavernia, T.E. Fischer, Near-Nanostructured WC-18 Pct Co Coatings with Low Amounts of Non-WC Carbide Phase: Part II. Hardness and Resistance to Sliding and Abrasive Wear, *Metall. Mater. Trans. A* 33(2002) 159-164.
- [74] J.K.N. Murthy, B. Venkataraman, Abrasive wear behaviour of WC–CoCr and Cr<sub>3</sub>C<sub>2</sub>–20(NiCr) deposited by HVOF and detonation spray processes, *Surf. Coat. Technol.* 200 (2006) 2642–2652.
- [75] P. Suresh Babu, B. Basu, G. Sundararajan, Abrasive wear behavior of detonation sprayed WC–12Co coatings: Influence of decarburization and abrasive characteristics, *Wear* 268 (2010) 1387–1399.



**List of figure captions**

Figure 1. Optical micrograph of a cracked Vickers indentation employed for fracture toughness measurement, with indication of horizontal crack lengths.

Figure 2. SEM micrographs of the cross-section of the W1 (A,C) and W2 (B,D) feedstock powders, with EDX microanalysis (E) acquired on the area marked in panel C.

Figure 3. XRD patterns of the W1 (A) and W2 (B) feedstock powders and of all corresponding WC-CoCr coatings.

Figure 4. Cross-sectional SEM micrographs of samples P1W1 (A,B), P2W1 (C,D), P3W1 (E,F), P4W1 (G,H).

Figure 5. Vickers microhardness results: boxplot representation of the distribution of 20 hardness values per coating following ASTM E-384-10, for samples belonging to the W1- (A) and W2- (B) series.

Figure 6. (A) Indentation fracture toughness ( $K_{IC}$ ) and (B) elastic modulus values of all coatings, with corresponding matrixes of  $p$ -values from Student's t-test. Sample pairs with  $p < 0.05$  are assumed to have significantly different average values and are highlighted in grey colour, whereas those with  $p \geq 0.05$  may have identical averages and are highlighted in white colour.

Figure 7. Wear rates and friction coefficients obtained by ball-on-disk dry sliding wear tests at room temperature (RT) and at 400 °C.

Matrixes of  $p$ -values from Student's  $t$ -test are provided for wear rate data at room temperature and at 400 °C. Sample pairs with  $p < 0.05$  are assumed to have significantly different average values and are highlighted in grey colour, whereas those with  $p \geq 0.05$  may have identical averages and are highlighted in white colour.

Figure 8. SEM micrographs of the wear scars on samples P1W1 (A) and P2W2 (B). Label 1 = plastically deformed “wavy” features; label 2 = areas with evidence of brittle cracking.

Figure 9. High magnification SEM micrographs of the wear scars of samples P2W2 (A) and P3W1 (B), showing details of brittle cracking regions, and of samples P1W2 (C) and P2W2 (D), showing details of plastically deformed “wavy” areas.

Figure 10. Results of principal component analysis for sliding wear at room temperature: (A) Pareto chart, and (B) plot of the variable coefficients (vectors) and of the observation scores (dots) along the 1<sup>st</sup> and 2<sup>nd</sup> principal components

Figure 11. Optical micrographs of the worn surface of the alumina ball after sliding at room temperature against WC-CoCr samples P1W1 (A) and P3W2 (B).

Figure 12. TEM micrographs of the loose wear debris collected outside the wear scar after ball-on-disk sliding wear testing on sample P1W2 (A,B), with inset SAED pattern, and EDX spectra acquired at the locations marked in panel A (D).

Note that the EDX peak of Cu is due to the contribution of the copper grid supporting the sample.

Figure 13. Raman spectra of the loose wear debris collected outside the wear scar after ball-on-disk sliding wear testing on sample P1W2.

Figure 14. SEM micrographs showing an overview (A) and a detail (B) of the wear scar produced after ball-on-disk testing on electroplated hard chromium at room temperature, and optical micrograph of the corresponding wear scar on the  $\text{Al}_2\text{O}_3$  ball (C).

Figure 15. TEM micrographs of the wear debris produced after ball-on-disk testing of the electroplated hard chromium layer at room temperature (A: overview; B: detail) and corresponding selected area diffraction pattern acquired on the area shown in panel B (C).

Figure 16. EDX spectra (A) and Raman spectra (B) acquired on the wear debris produced by ball-on-disk testing of electroplated hard chromium at room temperature.

Figure 17. SEM micrographs of the top surfaces of samples P3W1 (A) and P3W2 (B) after ball-on-disk wear testing at 400 °C.

Figure 18. SEM micrographs of the polished cross-sections of samples P1W2 (A: low-magnification, C: high magnification) and P3W1 (B: low-magnification, D: high magnification) after ball-on-disk wear testing at 400 °C.

The circles in panel D indicate areas with visible precipitates around the WC grains.

Figure 19. Schematics of thermal stress build-up in the coating – substrate system.

Figure 20. SEM micrographs of wear scars after ball-on-disk tests at 400 °C: overview of sample P1W1 (A), detail of cracks (arrows) on samples P1W1 (B) and P2W1 (C) and detail of adhesive delaminations on sample P1W1 (D).

Figure 21. SEM micrograph (A), AFM map (B) and Raman spectrum (C) acquired on the surface of sample P1W1 after ball-on-disk testing at 400 °C, outside the wear scar.

All Raman peaks labelled in panel (C) are ascribed to  $\text{WO}_3$  according to [62].

Figure 22. Optical micrograph of the wear scar on the  $\text{Al}_2\text{O}_3$  counterpart after ball-on-disk testing against sample P4W2 at 400 °C.

Figure 23. Volume losses of all samples after dry sand-rubber wheel testing.

Figure 24. Results of principal component analysis for abrasive wear testing: (A) Pareto chart, and (B) plot of the variable coefficients (vectors) and of the observation scores (dots) along the 1<sup>st</sup> and 2<sup>nd</sup> principal components.

Figure 25. SEM micrographs of wear scars produced by dry sand-rubber wheel testing: overviews of samples P1W1 (A) and P4W2 (B) and details of samples P1W1 (C) and P3W1 (D). The circles indicate lamellar detachments.

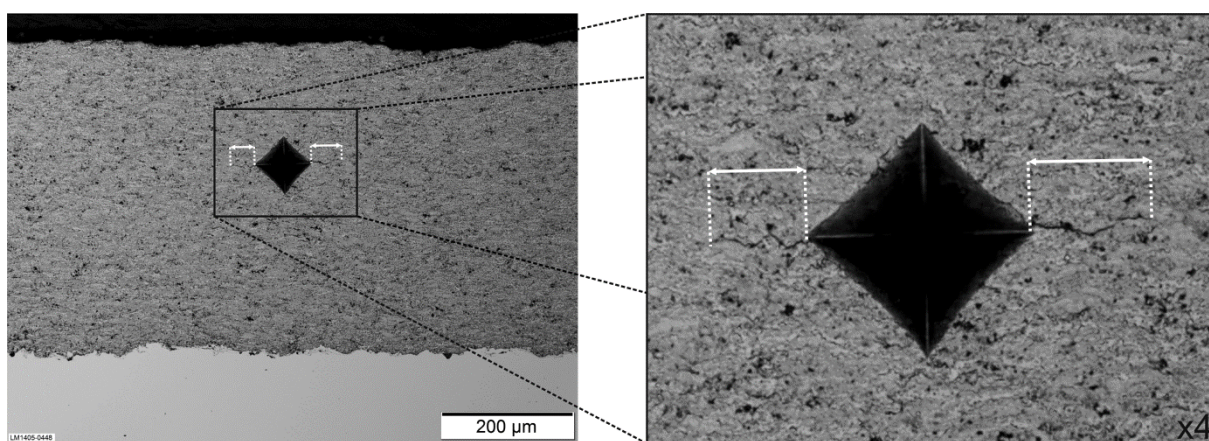


Fig 1

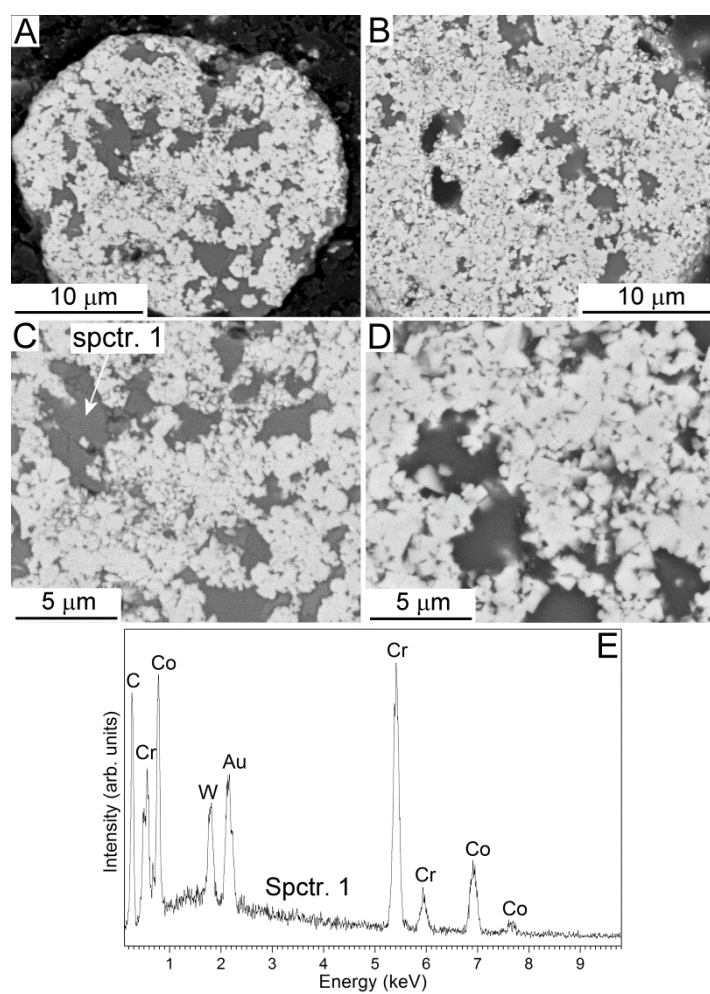


Figure 2

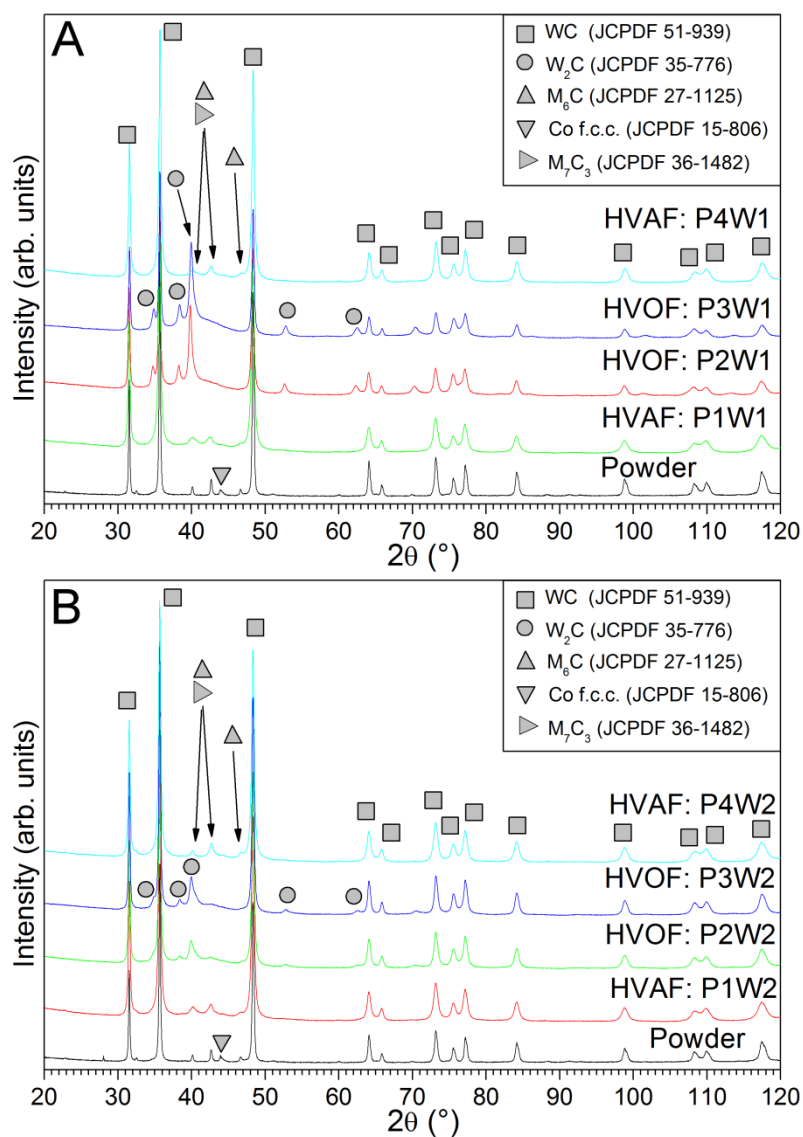


Figure 3

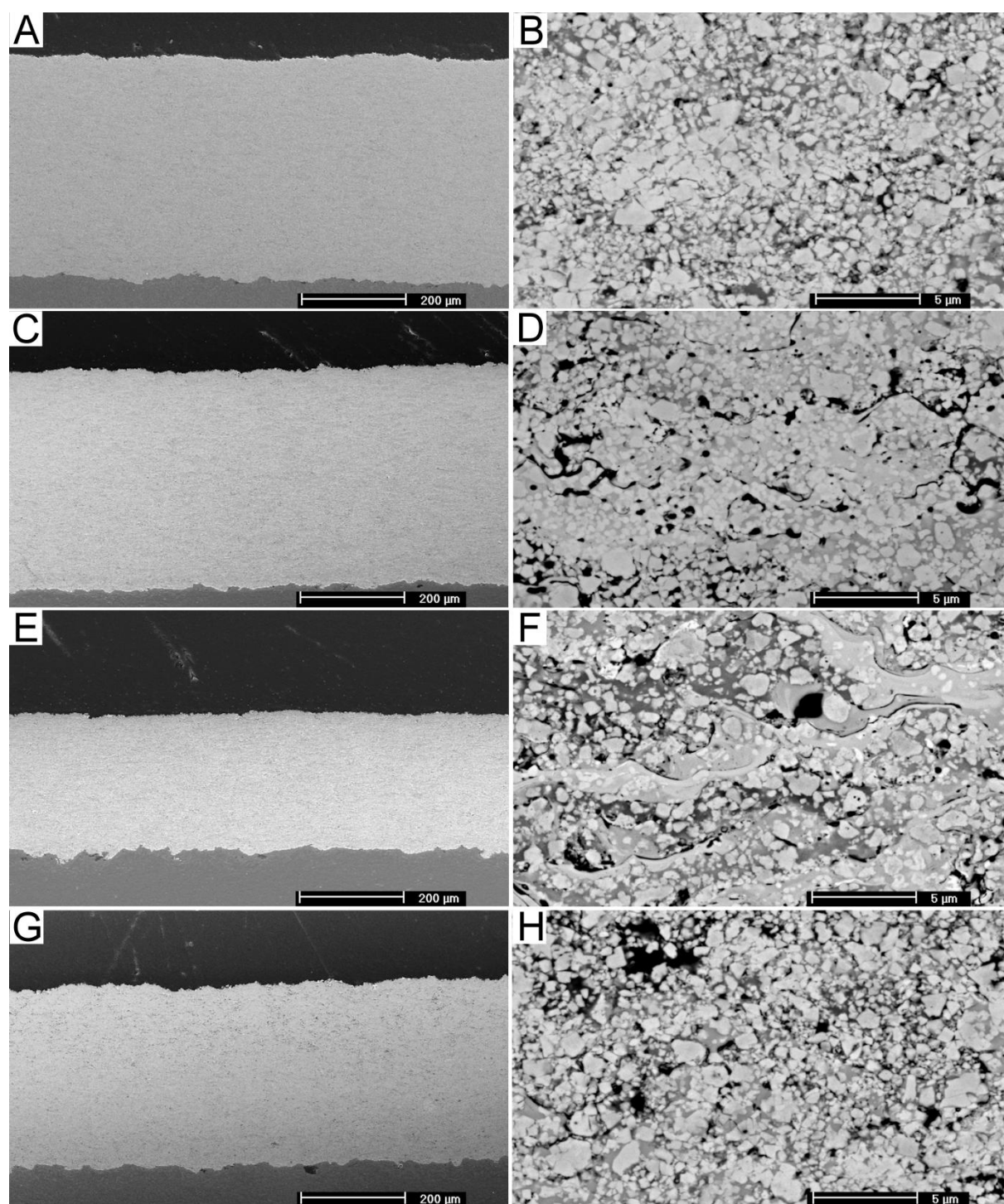


Figure 4



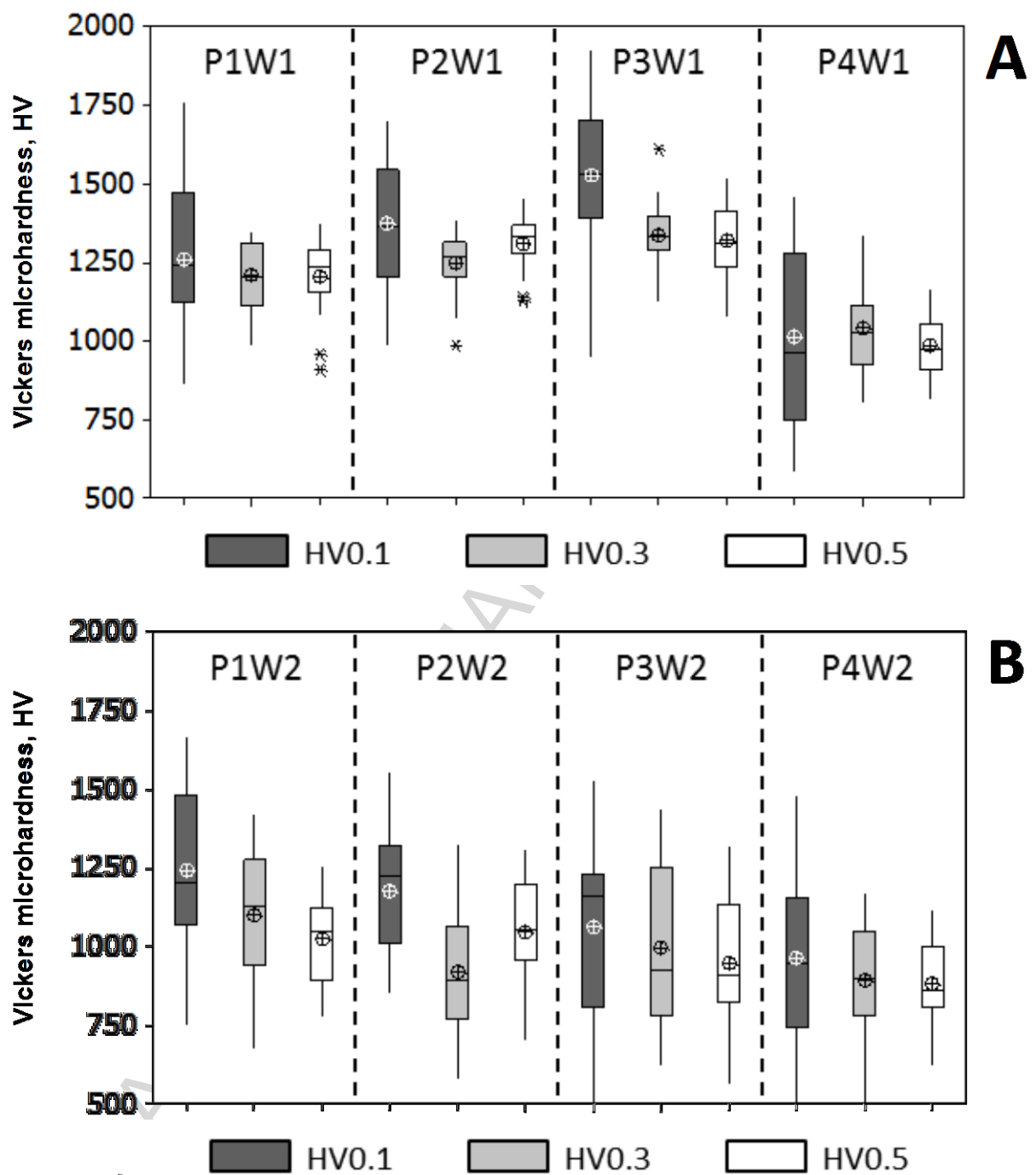


Fig 5

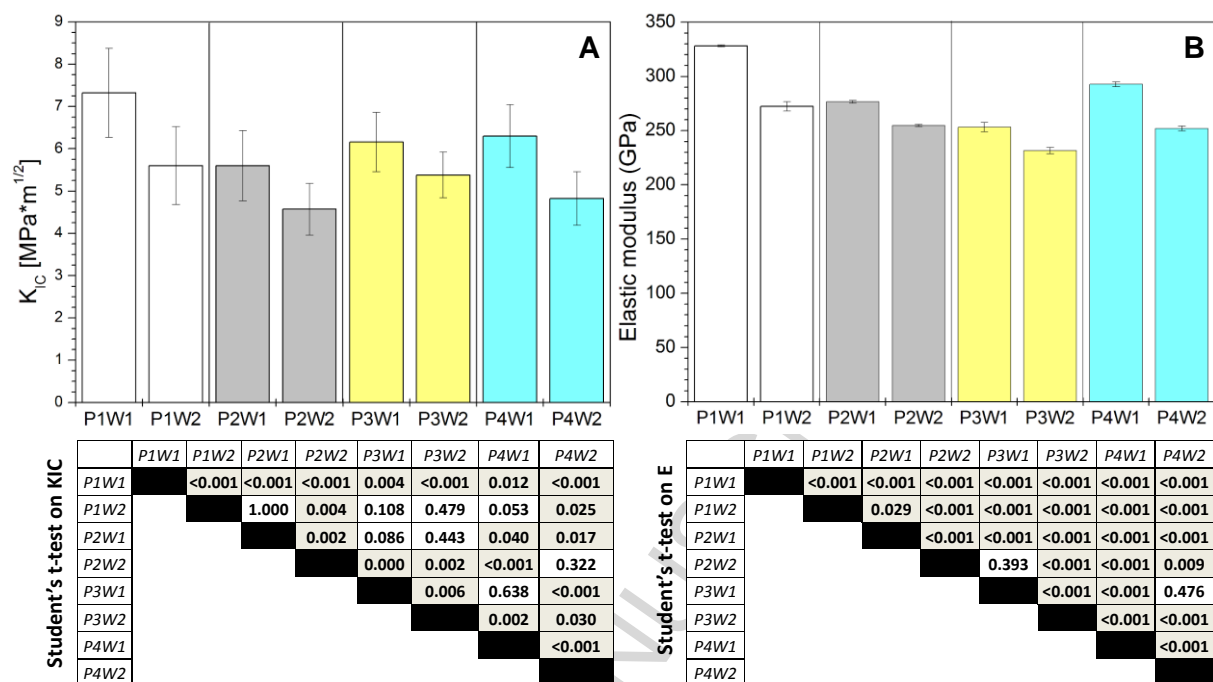


Figure 6

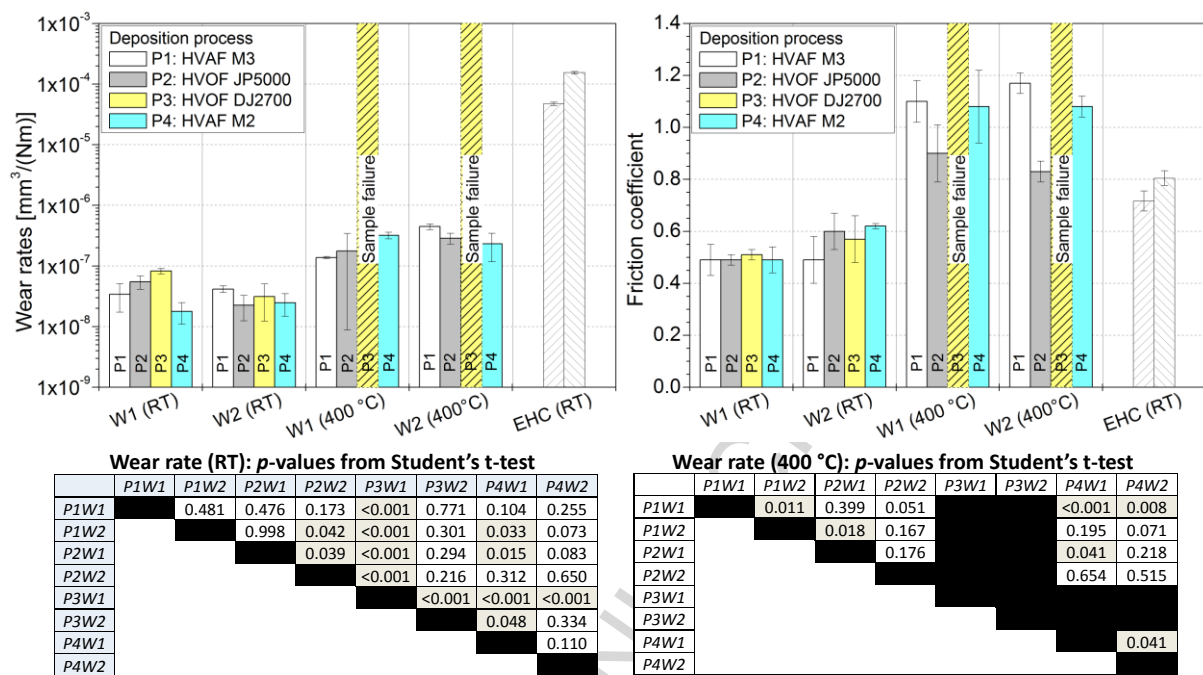


Figure 7

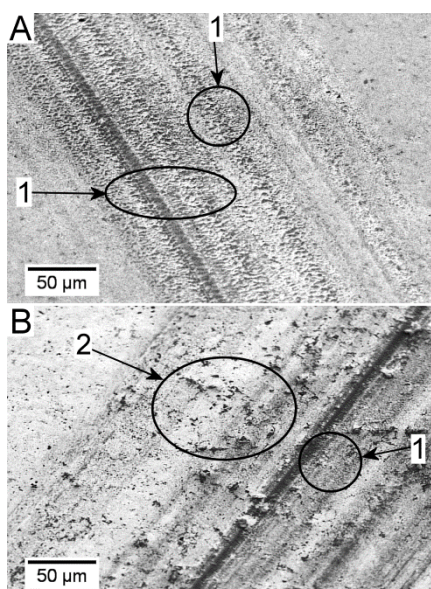


Figure 8

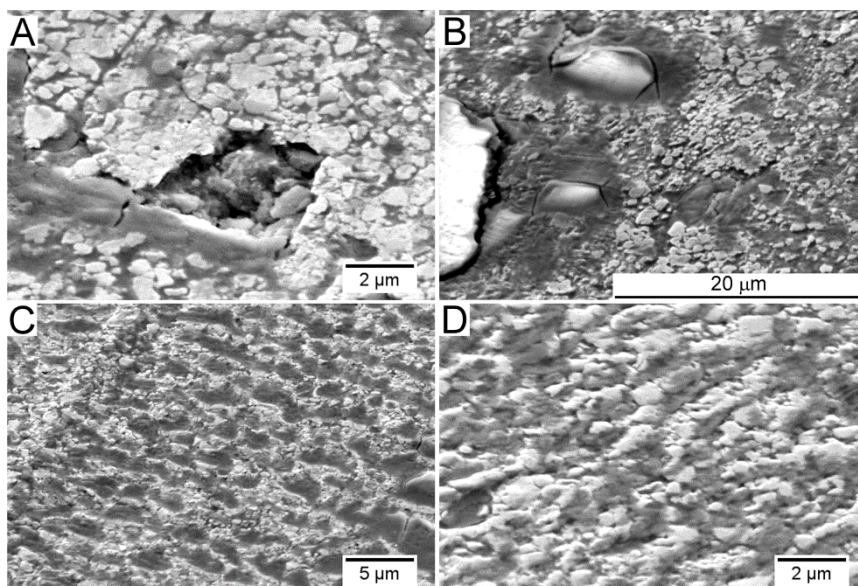


Figure 9

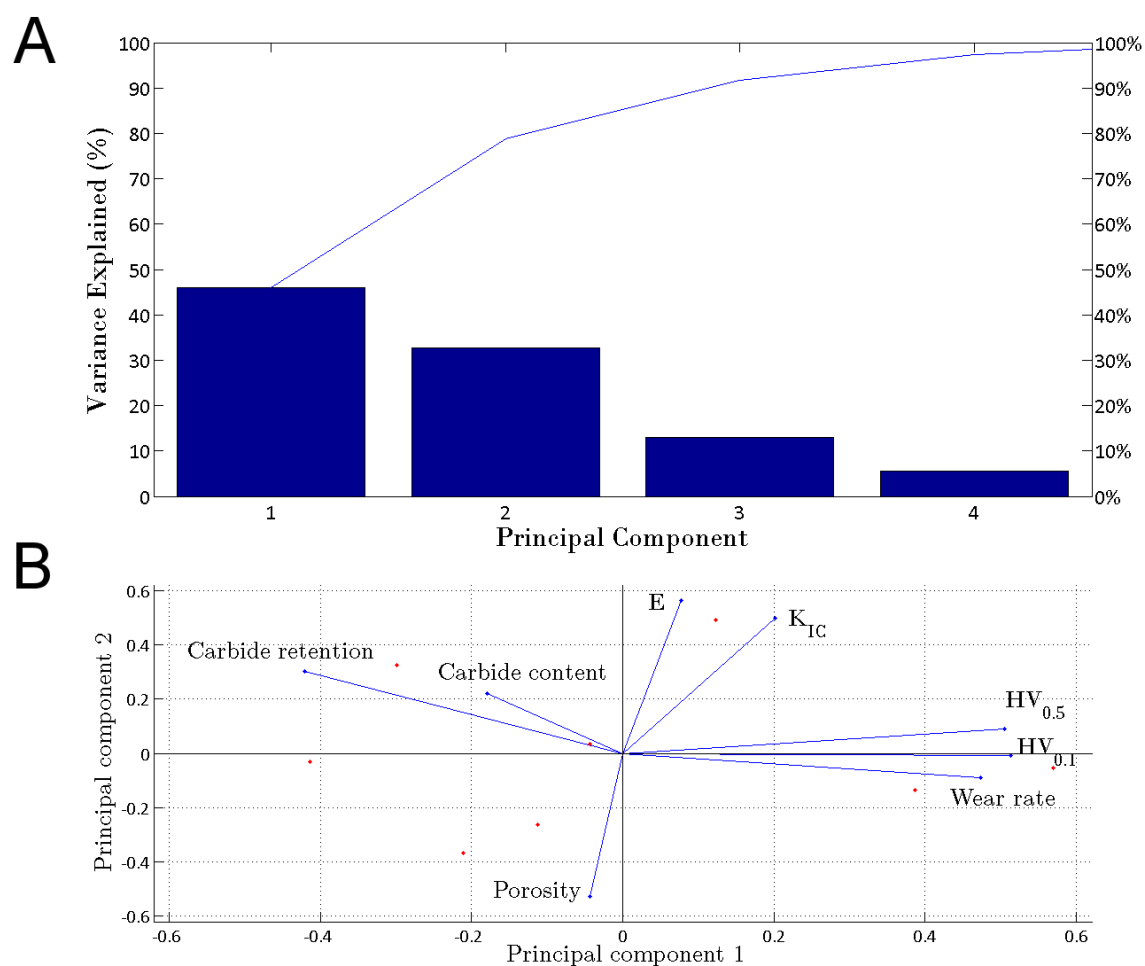


Figure 10

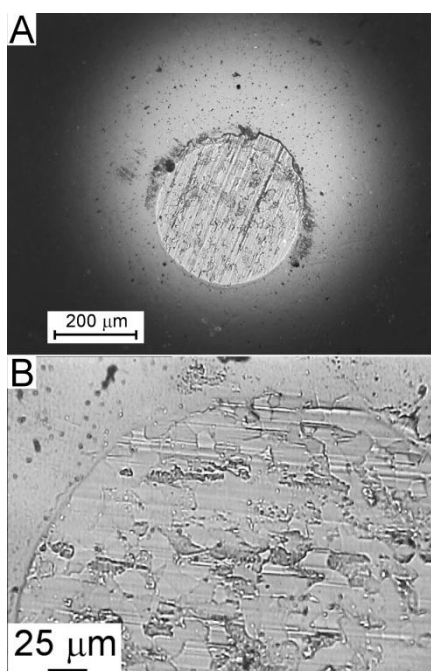


Figure 11

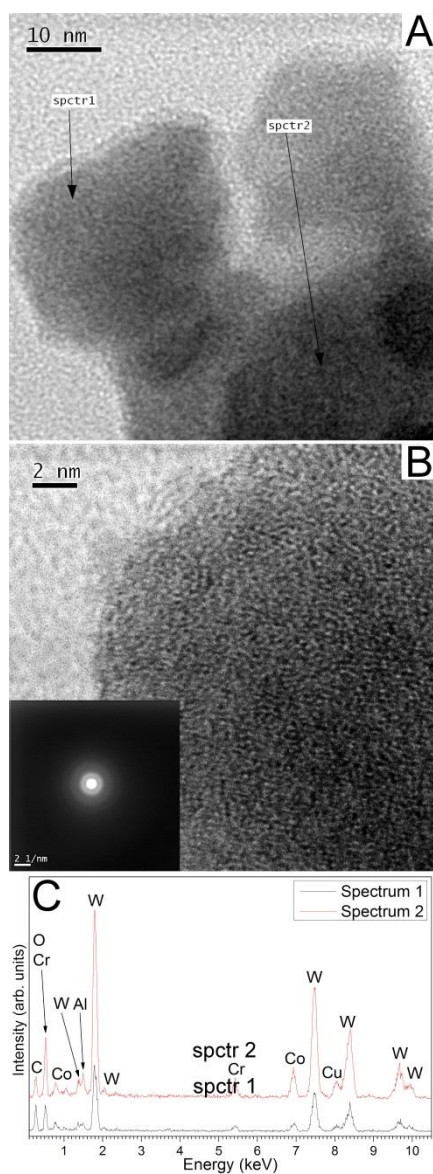


Figure 12



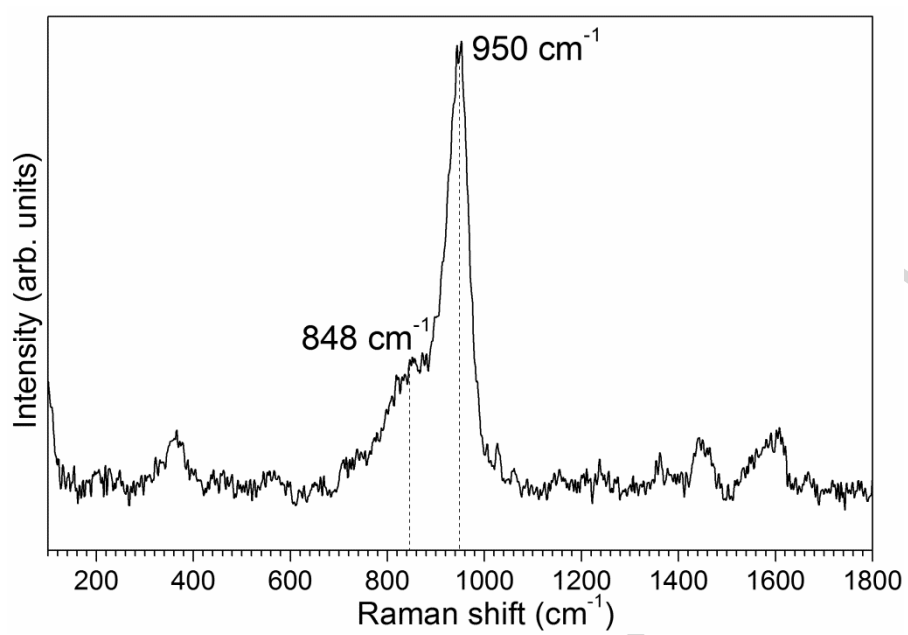


Figure 13

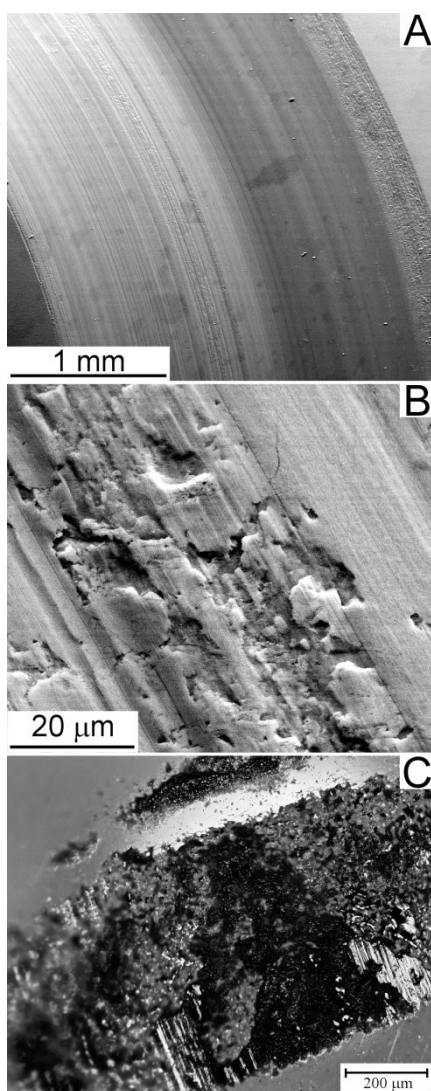


Figure 14

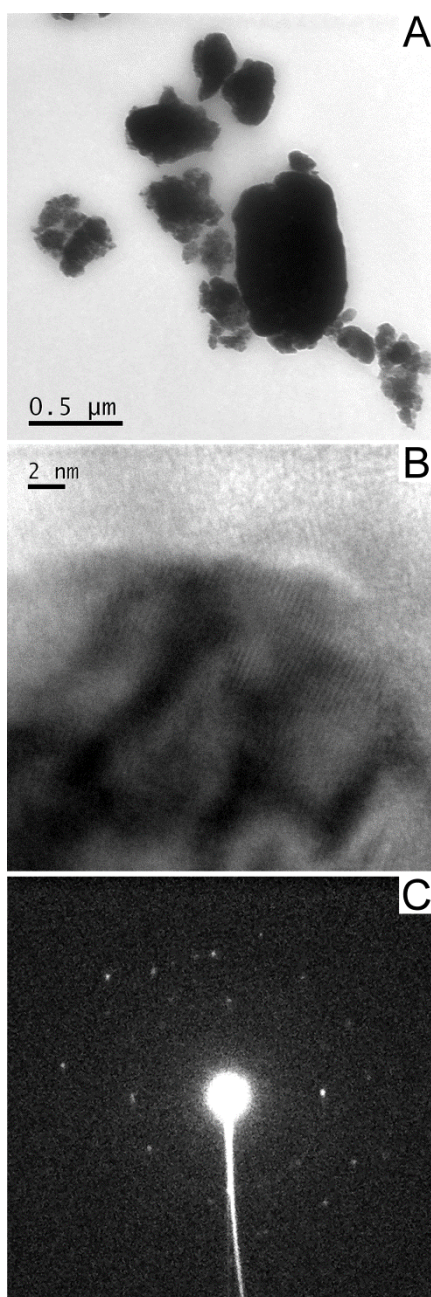


Figure 15

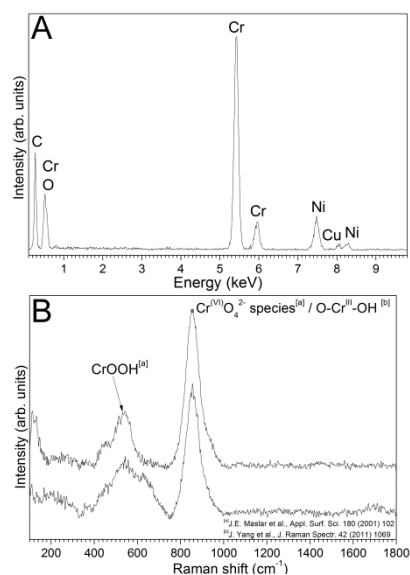


Figure 16

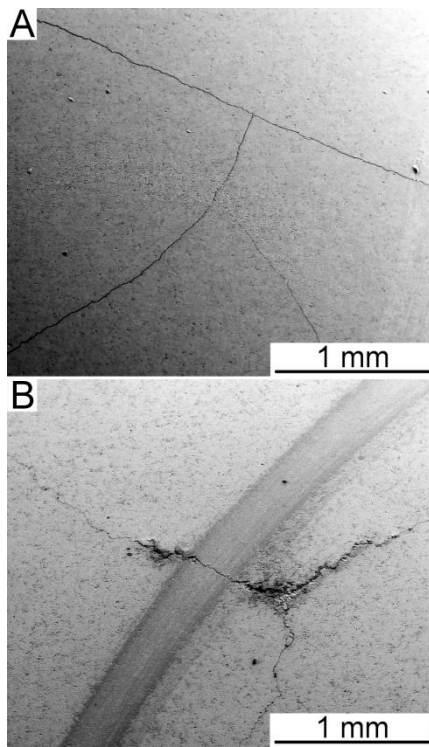


Figure 17

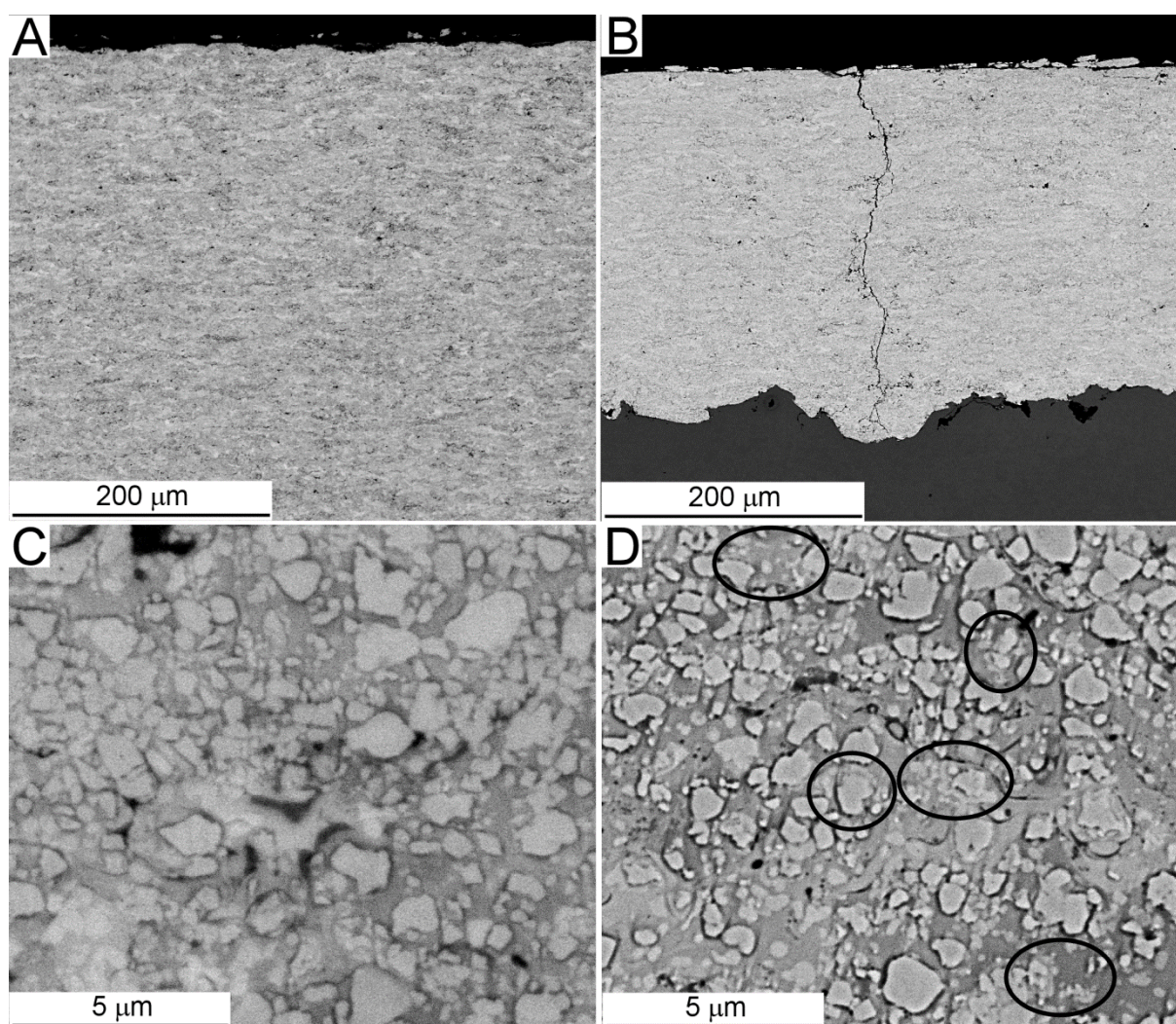


Figure 18

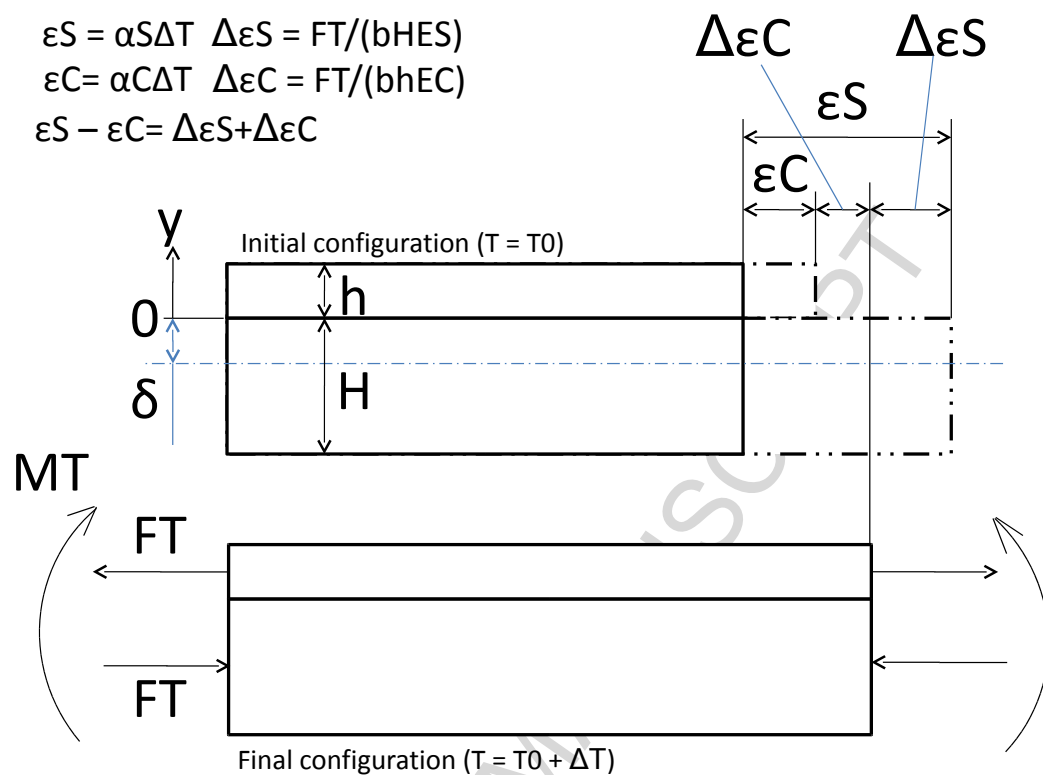


Figure 19



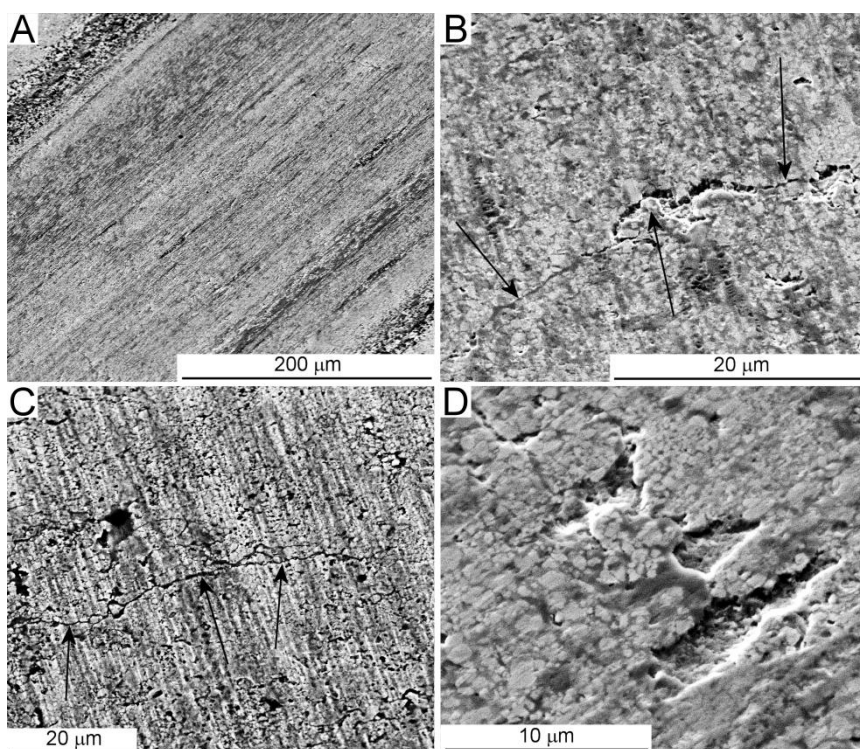


Figure 20



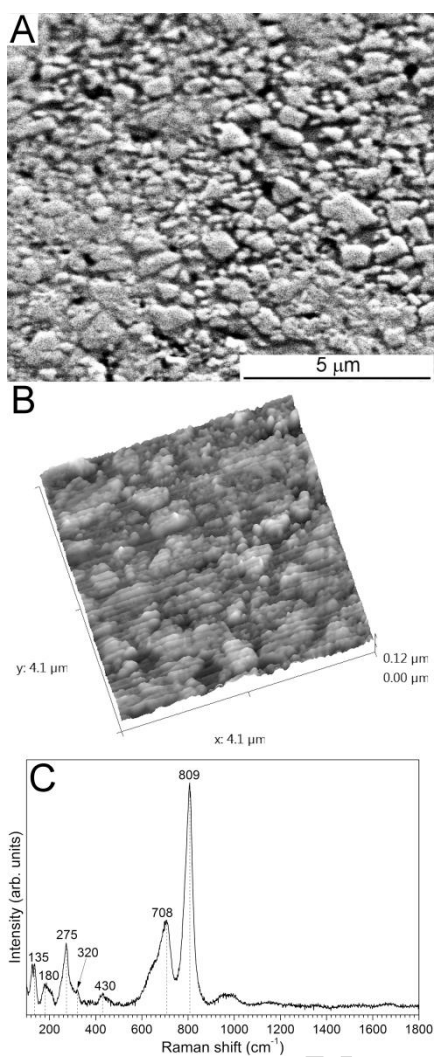


Figure 21

Figure 22

ACCEPTED MANUSCRIPT

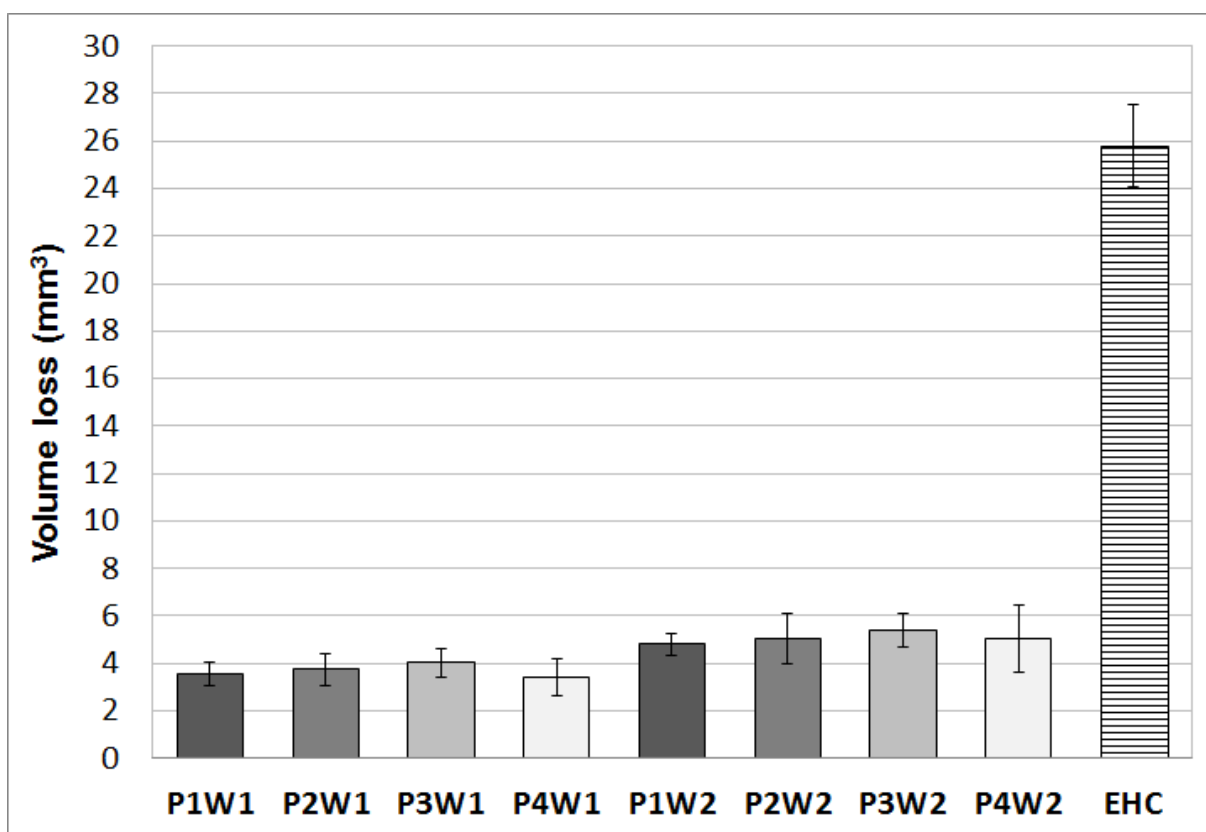


Figure 23

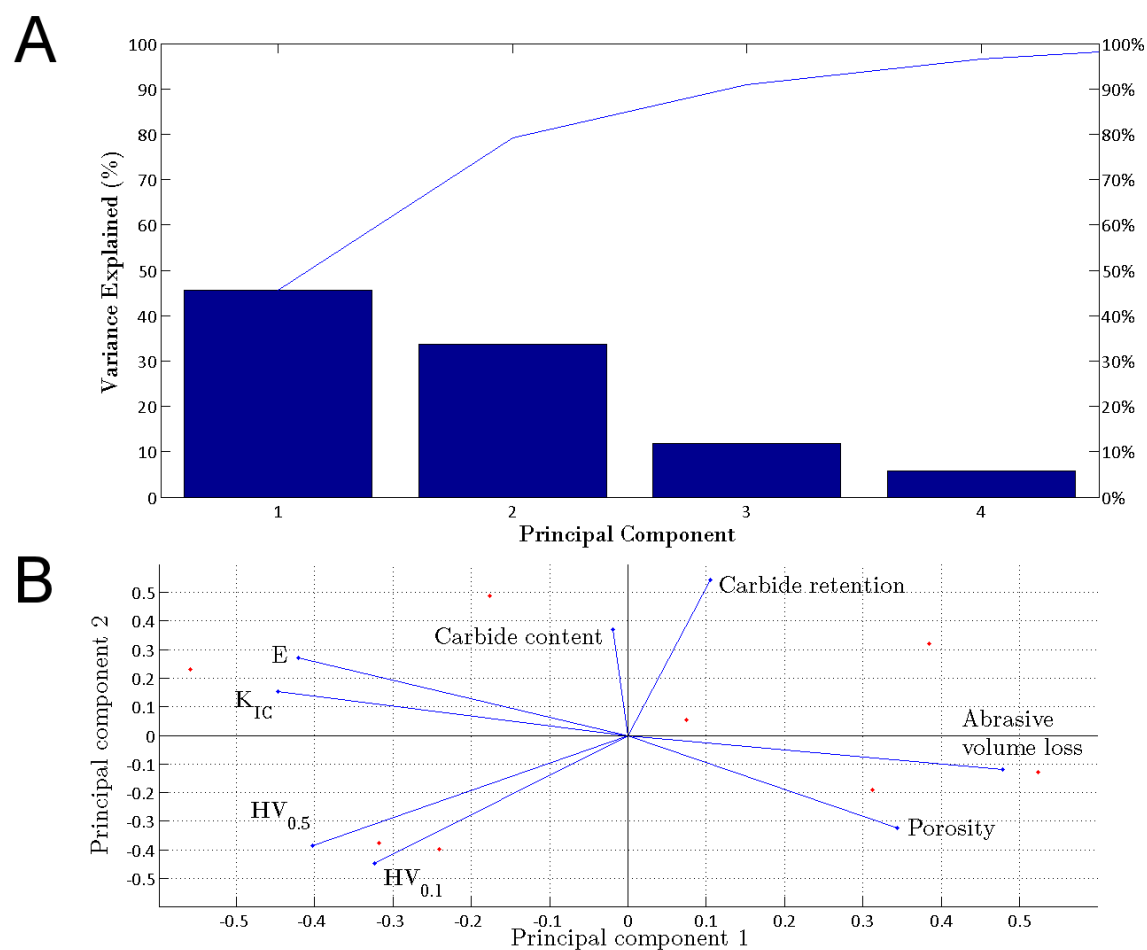


Figure 24

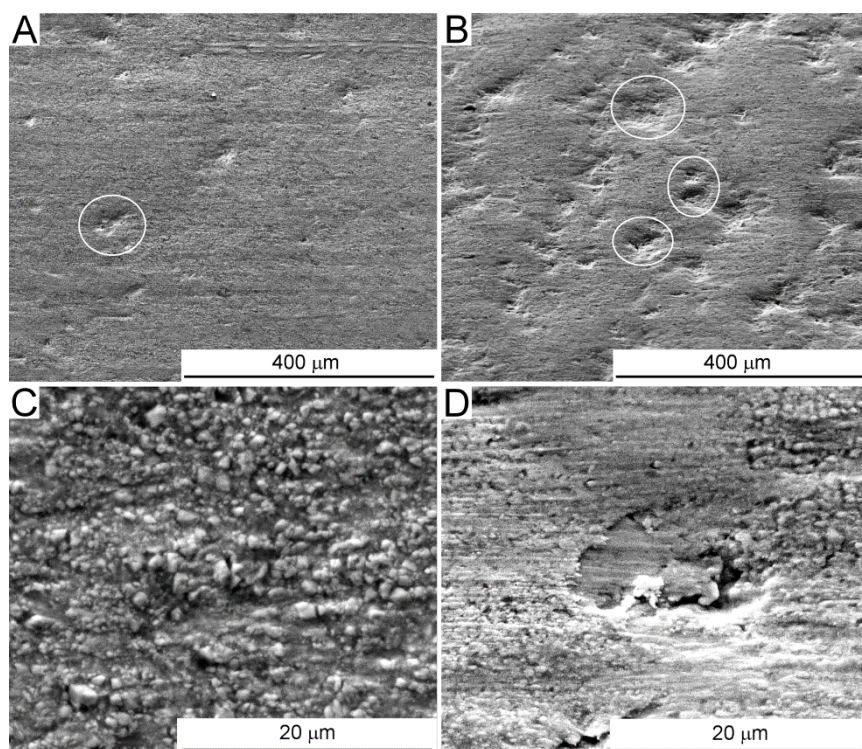


Figure 25

# Tables

Table I. List of powders, deposition techniques and resulting coatings used in this study, together with their conventional designations.

Powder Material				Deposition process (designation)			
Composition (wt.%)	Commercial designation	Size (μm)	Ref. code	HVAF M3 <sup>a)</sup> (P1)	HVOF JP5000 <sup>b)</sup> (P2)	HVOF DJ2700 <sup>c)</sup> (P3)	HVAF M2 <sup>d)</sup> (P4)
WC-Co-Cr 86-10-4	AMPERIT® <sup>e)</sup> 558.059	-30+5	W1	P1-W1	P2-W1	P3-W1	P4-W1
	AMPERIT® <sup>e)</sup> 558.074	-45+15	W2	P1-W2	P2-W2	P3-W2	P4-W2

<sup>a)</sup> M3-HVAF torch, Uniquecoat, Oilville, Virginia, USA

<sup>b)</sup> JP5000 torch, Praxair-Tafa, Concord, NH, USA

<sup>c)</sup> Diamond Jet 2700, Sulzer-Metco, Wohlen, Switzerland

<sup>d)</sup> M2-HVAF torch, Uniquecoat, Oilville, Virginia, USA

<sup>e)</sup> H.C. Starck GmbH, Laufenburg, Germany

Table II: index of carbide retention porosity (*I*) of all hardmetal coatings; volume fractions of matrix and of WC grains and average size of the latter, assessed by image analysis on SEM micrographs (Section 2.2); and resulting values of computed density (Section 2.3).

Sample	Porosity (vol.%)	Carbides (vol.%)	Carbide size (μm)	Binder (vol.%)	Density (g/cm <sup>3</sup> )	Index of WC retention ( <i>I</i> )
P1W1	0.7 ± 0.5	54.9 ± 9.0	0.7 ± 0.1	44.4 ± 8.9	12.4	> 98%
P1W2	2.1 ± 1.7	51.3 ± 7.0	0.8 ± 0.1	46.6 ± 6.6	12.1	> 98%
P2W1	3.9 ± 1.9	49.5 ± 4.7	0.6 ± 0.1	46.6 ± 4.7	11.8	60%
P2W2	4.1 ± 1.8	47.3 ± 5.9	0.6 ± 0.1	48.6 ± 5.5	11.6	84%
P3W1	2.0 ± 0.9	63.3 ± 9.5	0.8 ± 0.2	34.7 ± 9.3	12.9	54%
P3W2	7.3 ± 3.3	57.8 ± 8.5	0.8 ± 0.1	34.9 ± 7.7	12.1	83%
P4W1	1.1 ± 1.0	72.9 ± 2.9	1.2 ± 0.2	26.0 ± 2.5	13.7	> 98%
P4W2	1.8 ± 1.6	67.4 ± 3.3	1.1 ± 0.2	30.8 ± 2.2	13.2	> 98%

Table III. Coefficient of thermal expansion of WC-CoCr and of the Domex 355 steel substrate as a function of temperature, from optical dilatometer measurements.

Temperature range [°C]	CTE [ $\cdot 10^{-6} \text{ }^{\circ}\text{C}^{-1}$ ]	
	<i>WC-CoCr</i>	<i>Domex 355 steel</i>
30 – 100	6.59	12.59
30 – 200	6.72	13.27
30 – 300	6.81	13.82
30 – 400	6.90	14.23



Table IV. Residual stresses in W1-series samples, measured by X-ray diffraction using equation set (1) (Section 2.4).

Direction 1 is parallel to the long side of the 100 x 50 mm rectangular plates; direction 2 is parallel to the short side.

<b>Sample</b>	$\sigma_{11}$ [MPa]	$\sigma_{22}$ [MPa]	$\tau_{12}$ [MPa]
P1W1 (HVAF)	91	2	44
P2W1 (HVOF)	57	148	9
P3W1 (HVOF)	328	282	23
P4W1 (HVAF)	-23	59	-61

**Highlights**

Systematic tribological study of state-of-the-art HVOF and HVAF WC-10Co4Cr coatings

Room temperature sliding: ductile flow vs. brittle fracture balance depends on decarburisation

At 400 °C, sliding wear rates increase 10-fold as WC is degraded by oxidation

Some HVOF coatings fail at 400 °C due to combined thermal and residual stresses

Feedstock powders with small particle size improve intersplat cohesion and abrasion resistance of the coatings